Multistable inflatable origami structures at the metre scale

https://doi.org/10.1038/s41586-021-03407-4

Received: 24 August 2020

Accepted: 1 March 2021

Published online: 21 April 2021

Check for updates

David Melancon[1,7], Benjamin Gorissen[1,7], Carlos J. García-Mora[1,2], Chuck Hoberman[3,4,5]✉ & Katia Bertoldi[1,3,6]✉

From stadium covers to solar sails, we rely on deployability for the design of large-scale structures that can quickly compress to a fraction of their size[1–4]. Historically, two main strategies have been used to design deployable systems. The first and most frequently used approach involves mechanisms comprising interconnected bar elements, which can synchronously expand and retract[5–7], occasionally locking in place through bistable elements[8,9]. The second strategy makes use of inflatable membranes that morph into target shapes by means of a single pressure input[10–12]. Neither strategy, however, can be readily used to provide an enclosed domain that is able to lock in place after deployment: the integration of a protective covering in linkage-based constructions is challenging and pneumatic systems require a constant applied pressure to keep their expanded shape[13–15]. Here we draw inspiration from origami—the Japanese art of paper folding—to design rigid-walled deployable structures that are multistable and inflatable. Guided by geometric analyses and experiments, we create a library of bistable origami shapes that can be deployed through a single fluidic pressure input. We then combine these units to build functional structures at the metre scale, such as arches and emergency shelters, providing a direct route for building large-scale inflatable systems that lock in place after deployment and offer a robust enclosure through their stiff faces.

Large, deployable structures should ideally (1) occupy the minimum possible volume when folded, (2) be autonomous when deploying, (3) lock in place after deployment, and (4) provide a structurally robust shell (if they are designed to define a closed environment). To satisfy all these requirements, here we present an approach with roots in the Japanese art of paper folding: origami. Extensively used in robotics[16–20], metamaterials[21–25] and structures[26–30], origami principles have the potential to lead to efficient large-scale deployable structures as they offer (1) a versatile crease-based approach to shape design[31–33], (2) an easy actuation through inflation, if enclosed[34–36], (3) self-locking capabilities when designed to support multiple energy wells[37–44], and (4) the possibility to create a protective environment through their faces. While previous origami systems have explored inflatability and multistability separately[34–44], here we show that these two properties can co-exist, unlocking an unprecedented design space of metre-scale inflatable structures that harness multistability to maintain their deployed shape without the need for continuous actuation (see schematics in Fig. 1a).

Triangular facets as a platform for bistable and inflatable structures

To create inflatable and bistable origami structures, we start by considering a triangular building block ABC and denote with α and β the internal angles enclosed by the edges AB–AC and AB–BC, respectively (Fig. 1b). The triangle initially lies in the x–y plane and is subsequently deployed through a rotation around its edge BC. As shown in Fig. 1b, this deployment results in the displacement w_A of vertex A along the z direction and a volume V_{ABC} under the triangle

$$V_{ABC} = \frac{w_A ||AB||^2}{6} \frac{\sin\alpha}{\sin(\alpha+\beta)} \sqrt{\sin^2\beta - \frac{w_A^2}{||AB||^2}}, \quad (1)$$

where $||AB||$ indicates the length of AB. By focusing on the x–y plane, through simple geometrical considerations, one can see that if $\beta \in [\pi/4 - \alpha/2, \pi/2 - \alpha]$, the projection of vertex A during the deployment intersects the circle circumscribed to the initial configuration (Fig. 1b) for a displacement w_A^c defined as

$$w_A^c = ||AB|| \sqrt{1 - \frac{\cos^2\beta}{\sin^2(\alpha+\beta)}}. \quad (2)$$

It follows from the inscribed angle theorem[45] that for $w_A = w_A^c$, the angle α is recovered on the x–y plane (see Supplementary Information section 1 for details). As such, if triangles of this type are used as building blocks to form origami polyhedra, the assembled systems will have two distinct compatible configurations: one flat (identified by $w_A = 0$) and one expanded (identified by $w_A = w_A^c$). By contrast, any configuration

[1]J. A. Paulson School of Engineering and Applied Sciences, Harvard University, Cambridge, MA, USA. [2]Department of Building Structures and Geotechnical Engineering, University of Seville, Seville, Spain. [3]Wyss Institute for Biologically Inspired Engineering Harvard University, Cambridge, MA, USA. [4]Hoberman Associates, New York, NY, USA. [5]Graduate School of Design, Cambridge, MA, USA. [6]Kavli Institute, Harvard University, Cambridge, MA, USA. [7]These authors contributed equally: David Melancon, Benjamin Gorissen. ✉e-mail: choberman@gsd.harvard.edu; bertoldi@seas.harvard.edu

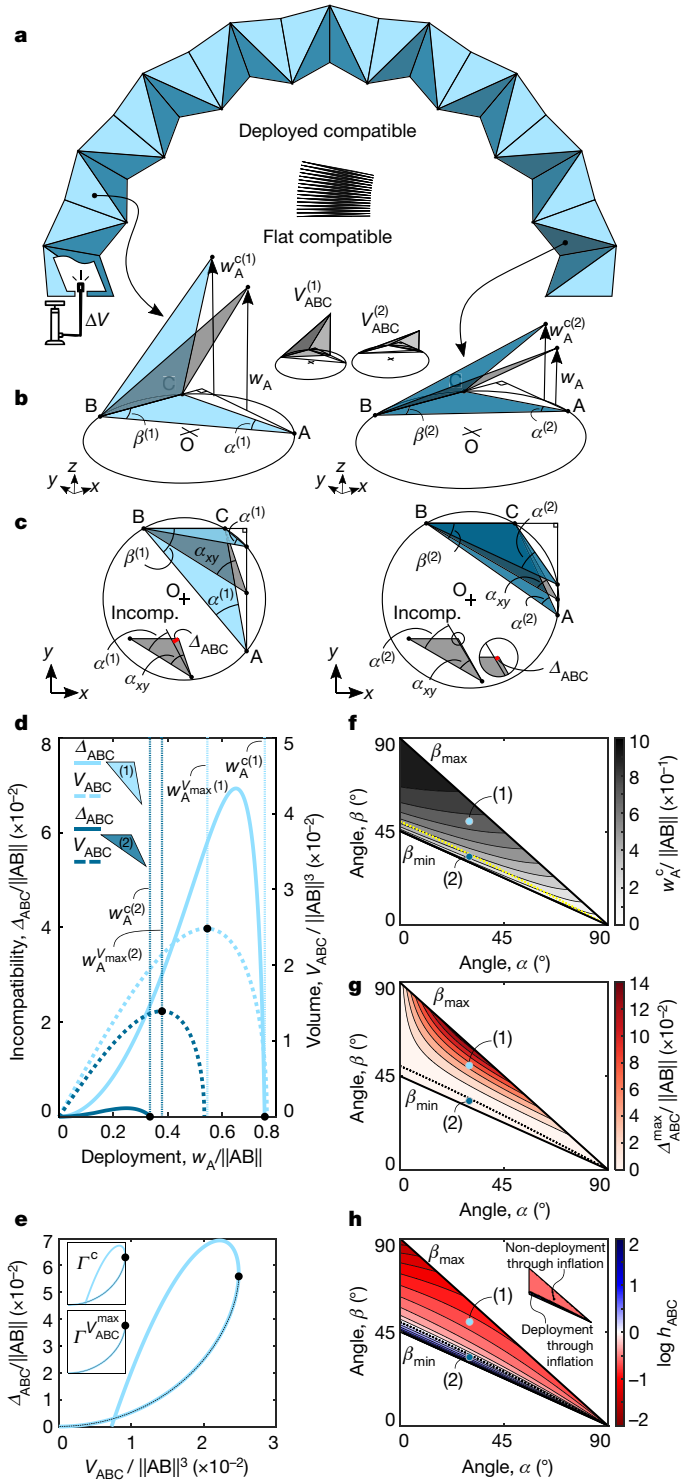

Fig. 1 | Triangular facets as building blocks for large-scale inflatable and bistable origami structures. a, Schematics illustrating the deployment via inflation of a large-scale origami structure comprising triangular facets. **b**, Deployment of two triangular building blocks ABC with angles $(\alpha^{(1)}, \beta^{(1)})$ and $(\alpha^{(2)}, \beta^{(2)})$. **c**, Projected view of the deployment showing the two intersection points with the circle centred in O. **d**, Evolution of incompatibility, Δ_{ABC}, and underlying volume, V_{ABC}, as a function of the deployment height, w_A. **e**, Evolution of incompatibility, Δ_{ABC}, as a function of the underlying volume, V_{ABC}. **f**–**h**, Contour maps of the compatible deployment height, w_A^c (**f**), maximum incompatibility, Δ_{ABC}^{max} (**g**) and inflation constraint, h_{ABC} (**h**).

with $0 < w_A < w_A^c$ will be geometrically frustrated, with incompatibility, Δ_{ABC}, that can be estimated as

$$\Delta_{ABC} = ||AC_{xy}|| \sin(\alpha_{xy} - \alpha), \quad (3)$$

where AC_{xy} and α_{xy} are the projection on the x–y plane of edge AC and angle α, respectively (note that $\alpha_{xy} = \alpha$ only for $w_A = 0$ and w_A^c; see the inset in Fig. 1c).

Therefore, to accommodate geometric frustration and realize closed origami shapes (that is, shapes forming a closed inflatable cavity) capable of switching between two compatible configurations, we connect stiff triangular building blocks to stretchable hinges. Importantly, whereas polyhedra composed of rigid triangular faces connected by perfect rotational hinges are known to be either rigid[46] or volume invariant during deployment[47,48], we anticipate our closed origami with stiff facets and flexible hinges to be bistable. Indeed, for hinges with low enough bending stiffness, we expect the energy profile of the closed origami to show two local minima corresponding to the flat and expanded compatible states (where the energy in the system can only be attributed to hinge bending), separated by an energy barrier caused by the deformation of the facets and the hinges required to accommodate geometric incompatibility.

To gain more insights into the behaviour of our building blocks, we focus on the deployment of two triangles with $(\alpha^{(1)}, \beta^{(1)}) = (30°, 50°)$ and $(\alpha^{(2)}, \beta^{(2)}) = (30°, 33°)$. In Fig. 1d, we report the evolution of the incompatibility, Δ_{ABC}, and the underlying volume, V_{ABC}, as a function of the deployment height, w_A, for both triangles. We find that the triangle with $\beta^{(1)} = 50°$ is characterized by both larger w_A^c and maximum incompatibility, $\Delta_{ABC}^{max} = \max(\Delta_{ABC})$. However, for this triangle, the expanded compatible state is located after the configuration corresponding to the maximum underlying volume ($w_A^{c(1)} > w_A^{V_{ABC}^{max}(1)}$) and, therefore, cannot be reached when V_{ABC} is controlled. As such, whereas we expect a closed origami structure realized using these triangles to have two stable states with very different internal volume, we cannot use inflation to switch between the two of them. By contrast, the triangle with $\beta^{(2)} = 33°$ exhibits much smaller Δ_{ABC}^{max} and w_A^c, but can be deployed when controlling the volume as $w_A^{c(2)} < w_A^{V_{ABC}^{max}(2)}$. This suggests that closed origami realized using this triangle can be deployed using inflation, but have an expanded configuration very similar to the flat one. Further, we expect such structures to be only marginally bistable, as small perturbations are enough to overcome the energy barrier associated with the small $\Delta_{ABC}^{max(2)}$.

Whereas in Fig. 1b–d we focus on two geometries, we next consider all deployable triangles (that is, triangles with $\pi/4 - \alpha/2 \le \beta \le \pi/2 - \alpha$) and look for those that can potentially lead to deployable structures that are simultaneously bistable and inflatable. Towards this end, we use w_A^c to estimate the change in shape between the compatible states and Δ_{ABC}^{max} to evaluate bistability (that is, to estimate the energy required to snap back from the expanded to the flat state). Furthermore, we introduce an inflation constraint

$$h_{ABC} = \frac{\Gamma^{V_{ABC}^{max}}}{\Gamma^c}, \quad (4)$$

where $\Gamma^{V_{ABC}^{max}}$ and Γ^c are the arc lengths measured on the Δ_{ABC}–V_{ABC} curve between the flat stable state and the state of maximum volume and between the flat and expanded stable configurations, respectively (Fig. 1e). It follows from equation (4) that only geometries with $\log h_{ABC} \ge 0$ can be deployed through fluidic actuation as those are the only ones for which the expanded compatible configuration is reached before the one with maximum volume during inflation (note that $\log h_{ABC} = -1.46$ and $\log h_{ABC} = 0.322$ for the two triangles considered in Fig. 1b, c).

In Fig. 1f–h, we report w_A^c, Δ_{ABC}^{max} and h_{ABC} for all deployable triangles. We find that both w_A^c and Δ_{ABC}^{max} are maximized in the region close

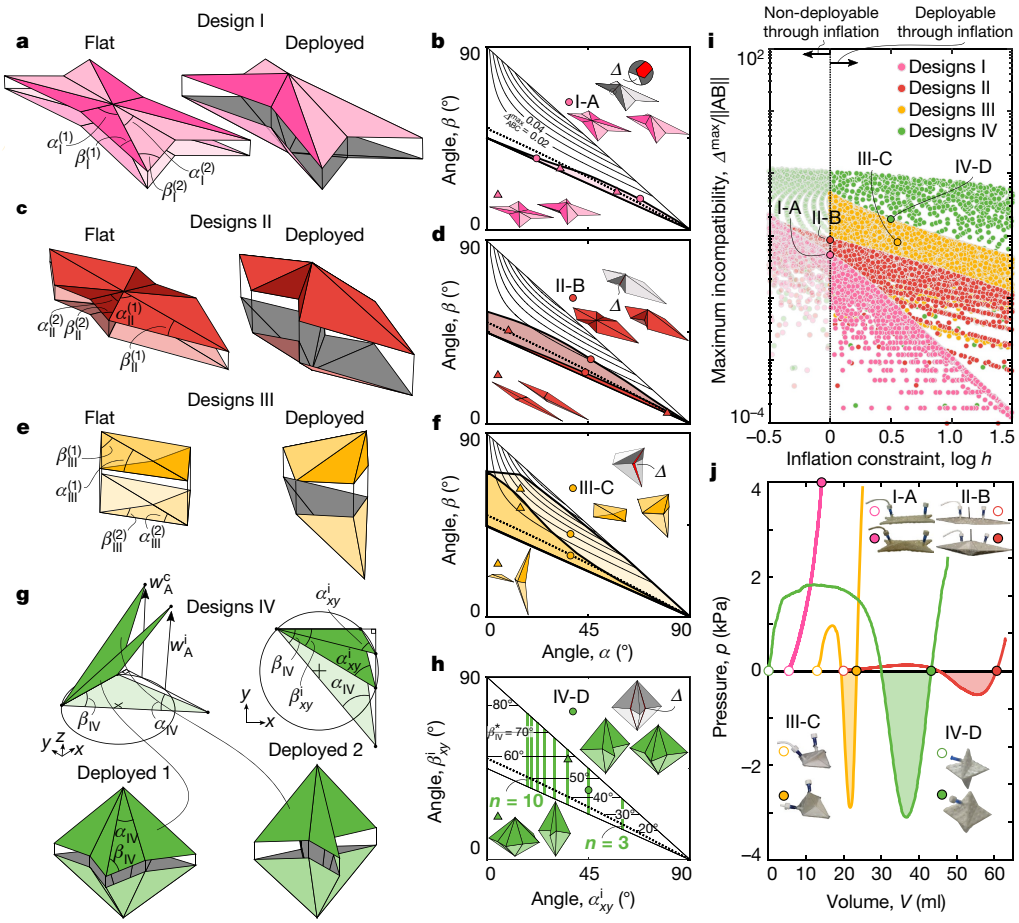

Fig. 2 | Bistable and inflatable origami shapes. a–f, Examples of Designs I (**a**, **b**), Designs II (**c**, **d**) and Designs III (**e**, **f**) geometries in both the flat and deployed stable configurations (**a**, **c**, **e**) along with the regions in the α–β space leading to inflatable structures (**b**, **d**, **f**). The bright and dark shaded regions in the plots represent the triangles with angles $(\alpha^{(1)}, \beta^{(1)})$ and $(\alpha^{(2)}, \beta^{(2)})$, respectively. The contour lines represent the maximum incompatibility of the triangular building blocks, Δ^{max}_{ABC}, the dashed line separates the region with positive and negative h_{ABC}. The solid circles and triangles indicate the triangular building blocks used to make the designs shown in the insets. **g**, Deployment of a triangular building block that has been initially rotated around its edge BC to have a height w^{i}_{A}. **h**, Contour map of angle β^{*}_{IV} required to obtain Designs IV that are both inflatable and bistable. **i**, Maximum incompatibility, Δ^{max}, versus the inflation constraint, h, for 500,000 random geometries of Designs I–IV. **j**, Pressure–volume curves recorded when testing our centimetre-scale prototypes. See Supplementary Information for the rationale behind geometry and material selection.

to the upper boundary of the domain (that is, when $\beta \to \pi/2 - \alpha$). By contrast, the triangles deployable through inflation (for which $\log h_{ABC} \geq 0$) are all close to the lower boundary of the domain (that is, when $\beta \to \pi/4 - \alpha/2$) and show small values of w^{c}_{A} and Δ^{max}_{ABC}. As such, these results indicate that we cannot realize closed origami structures that are at the same time bistable and inflatable using a single triangle building block.

Extending the design space to enable deployment via inflation

In an attempt to realize inflatable closed origami structures with stable flat and expanded configurations, we turn our focus to systems realized by assembling two different triangles with internal angles $(\alpha^{(1)}, \beta^{(1)})$ and $(\alpha^{(2)}, \beta^{(2)})$. To begin with, we arrange $2n$ triangles of each type to form two identical layers with n-fold symmetry and connect them at their outer boundaries (Fig. 2a, c). The resulting star-like structures (reminiscent of an origami waterbomb base[38,49]) define an internal volume $V = 2n(V^{(1)}_{ABC} + V^{(2)}_{ABC})$, exhibit geometric incompatibility $\Delta = 2n(\Delta^{(1)}_{ABC} + \Delta^{(2)}_{ABC})$ and are inflatable only if $\log h = \log(\Gamma^{V^{max}}/\Gamma^{c}) \geq 0$, where $\Gamma^{V^{max}}$ and Γ^{c} are the arc lengths measured on the Δ–V curve between the states with $V = 0$ and $V = V^{max} = \max(V)$ and between the two stable configurations, respectively. However, it is important to note that to realize these star-like structures, the pair of triangles cannot be arbitrarily chosen. This is because geometric compatibility is guaranteed only if the two triangles have (1) identical deployed compatible height (that is, $w^{c(1)}_{A} = w^{c(2)}_{A}$), (2) connecting deployed edges (either AB or AC) of equal length, and (3) angles that satisfy $\alpha^{(1)} + \alpha^{(2)} = \pi/n$.

As shown in Fig. 2a, we first connect the two triangles via their longest edge ($||AB^{(1)}|| = ||AB^{(2)}||$) and refer to these structures as Designs I. We identify all possible geometries by enforcing requirements 1–3 and find that designs deployable through inflation (for which $\log h \geq 0$) not only have a deployed shape almost indistinguishable from the initial flat one (see insets of structures in Fig. 2b) but also are made of two triangles with very low Δ^{max}_{ABC} (see area highlighted in magenta in Fig. 2b). As such, the inflatable Designs I exhibit very low maximum incompatibility $\Delta^{max} = \max(\Delta)$ (see magenta markers in Fig. 2i for 500,000 randomly chosen geometries). To investigate the performance of these inflatable designs, we fabricate and test the geometry with $\log h \geq 0$ and the highest Δ^{max} (Design I-A with $(\alpha^{(1)}_{I\text{-}A}, \beta^{(1)}_{I\text{-}A}) = (22°, 35°)$ and $(\alpha^{(2)}_{I\text{-}A}, \beta^{(2)}_{I\text{-}A}) = (68°, 14°)$ for which $\Delta^{max}/||AB|| = 2.67 \times 10^{-2}$; see magenta circular marker in Fig. 2i). A centimetre-scale prototype with $||AB^{(1)}|| = ||AB^{(2)}|| = 60$ mm is constructed by connecting three-dimensional-printed stiff triangular facets with compliant hinges made of thin polyester sheets and an inflatable cavity is formed by coating it with a 0.5-mm-thick layer of silicone rubber (see insets in Fig. 2j, Supplementary Information section 2, Supplementary Video 1 for details).

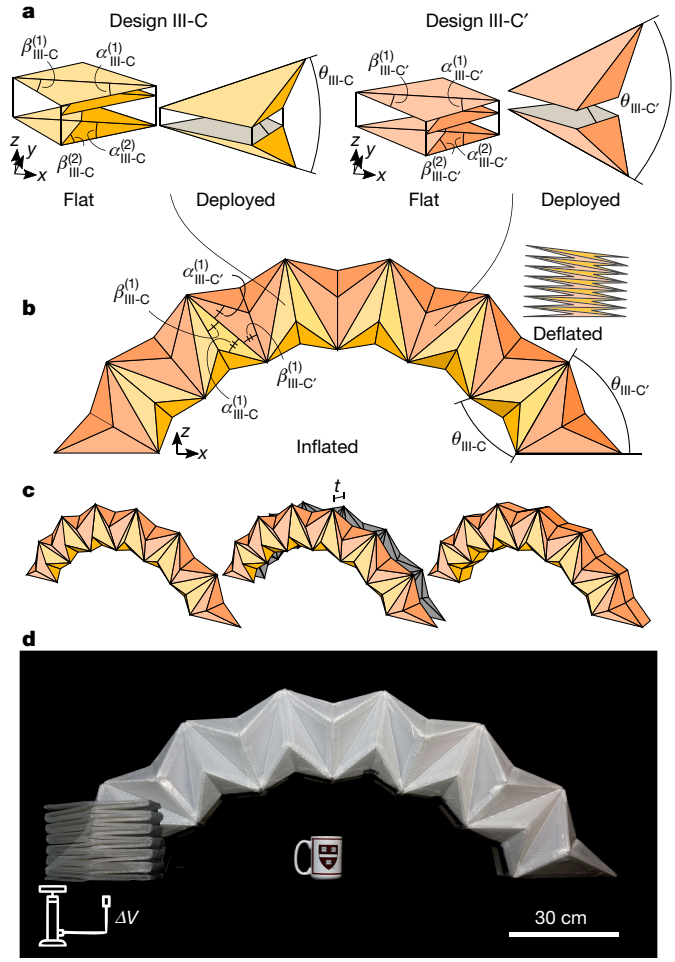

Fig. 3 | Metre-scale inflatable archway. a, The two Design III units used to construct the arch. **b**, Schematics illustrating an inflatable archway comprising six Design III-C and seven Design III-C′ units. **c**, To facilitate inflation, we create a single cavity by cutting all units through their x–z mirror plane, separating the two resulting parts by a distance t, and connecting them with rectangular facets. **d**, Fabricated metre-scale inflatable arch in its flat and deployed stable configurations.

The sample is then deployed by supplying water at a constant rate of 10 ml min^{-1} with a syringe pump, while monitoring the pressure with a pressure sensor (see Supplementary Information section 3 for details). We find that the pressure, p, increases monotonically with V until the maximum volume for the cavity is reached (Fig. 2j, Supplementary Video 2). As such, our test reveals that the Δ^{max} of this design is not large enough to make the fabricated structure bistable.

Next, with the goal of increasing the geometric incompatibility of the inflatable designs, we investigate the response of star-like structures in which the longest edge of one triangle, AB$^{(1)}$, is connected to the shortest edge of the other one, AC$^{(2)}$ (we refer to these designs as Designs II; Fig. 2c). Again, we impose requirements 1–3 to identify all possible geometries and find that those deployable through inflation comprise two very distinct triangles: a first one with low Δ^{max}_{ABC} but $\log h^{(1)}_{ABC} > 0$ (see area highlighted in dark red in Fig. 2d) and a second one with substantially larger Δ^{max}_{ABC} but $\log h^{(2)}_{ABC} < 0$ (see area highlighted in bright red in Fig. 2d). Remarkably, we find that the combination of these different triangles results in inflatable designs with higher maximum incompatibility compared with Designs I (see red markers in Fig. 2i for 500,000 randomly chosen geometries). As a result, when we fabricate and test the inflatable geometry that maximizes Δ^{max} (Design II-B with $(\alpha^{(1)}_{II\text{-}B}, \beta^{(1)}_{II\text{-}B}) = (43.6^\circ, 25.2^\circ)$ and $(\alpha^{(2)}_{II\text{-}B}, \beta^{(2)}_{II\text{-}B}) = (46.4^\circ, 33.5^\circ)$ for which $\Delta^{max}/||AB|| = 8.58 \times 10^{-2}$; see red marker in Fig. 2i), we observe a negative pressure region (see red curve in Fig. 2j, Supplementary Video 2). This confirms the presence of an expanded stable configuration that can be reached through fluidic actuation (see Supplementary Fig. 23 for details) and indicates the existence of a threshold value of $\Delta^{max}/||AB||$ (dependent on materials and fabrication process) that marks the transition from monostable to bistable behaviour.

Whereas the connection of two different triangles side by side enables us to design inflatable and bistable structures, it limits us to star-like shapes. To expand the range of shapes, we next arrange the two triangles on top of each other in the flat configuration and mirror them twice to form an inflatable cavity (we refer to these structures as Designs III; Fig. 2e). This leads to geometries comprising eight triangles that are initially flat and transform into wedge-like shapes upon deployment. As for Designs I and Designs II, geometric compatibility for Designs III requires a pair of triangles with $w^{c(1)}_A = w^{c(2)}_A$ and $||AB^{(1)}|| = ||AC^{(2)}||$, but the closure of the cavity is only possible if $\alpha^{(1)}_{III} = \alpha^{(2)}_{III}$. By imposing these constraints and $\log h \geq 0$, we find that inflatable Designs III can be realized by combining two triangles with $\log h_{ABC} < 0$ and, therefore, substantially larger Δ^{ABC}_{max} (see areas highlighted in yellow in Fig. 2f). This is because the internal volume of Designs III is defined by the difference between $V^{(1)}_{ABC}$ and $V^{(2)}_{ABC}$ (that is, $V = 4(V^{(1)}_{ABC} - V^{(2)}_{ABC})$) instead of their sum, as for Designs I and Designs II. Importantly, by plotting Δ^{max} versus h for 500,000 randomly chosen Designs III, we find that these geometries are characterized by much larger maximum incompatibility in the inflatable domain. As a result, when we fabricate and test Design III-C with $(\alpha^{(1)}_{III\text{-}C}, \beta^{(1)}_{III\text{-}C}) = (37.1^\circ, 30.0^\circ)$ and $(\alpha^{(2)}_{III\text{-}C}, \beta^{(2)}_{III\text{-}C}) = (37.1^\circ, 40.6^\circ)$, (for which $\Delta^{max}/||AB|| = 9.93 \times 10^{-2}$), we record even larger values of negative pressure (that is, larger energy barrier preventing the snap back) compared with the previous bistable Design II-B (Fig. 2j, Supplementary Video 2).

So far, all identified designs (that is, Designs I–III) have been realized by assembling triangles that initially lie in the x–y plane and recover their angle α on such a plane for $w_A = w^c_A$. However, the triangle in the x–y plane can also be seen as the projection of a triangle with internal angles α and β that has been initially rotated around its edge BC to have a height w^i_A and projected angles α^i_{xy} and β^i_{xy} (Fig. 2g). In this case, if $\beta^i_{xy} \in [\pi/4 - \alpha^i_{xy}/2, \pi/2 - \alpha^i_{xy}]$ the angle α^i_{xy} is preserved for two distinct deployment heights, w^i_A and w^c_A (see inset in Fig. 2g, Supplementary Information section 1 for details). As such, we can use these triangles as building blocks to realize star-like origami shapes with two expanded stable configurations corresponding to w^i_A and w^c_A. An interesting feature of this family of structures (which we refer to as Designs IV) is that if we select $\alpha^i_{xy} = \pi/n$ ($n = 3, 4, \ldots$) and

$$\beta_{IV} \geq \beta^*_{IV} = \tan^{-1}(\sqrt{2}\ \tan\beta^i_{xy}), \tag{5}$$

β^*_{IV} denoting a critical threshold value, the resulting origami are bistable and inflatable, even if made out of a single triangular building block (see Supplementary Information section 1 for details). This is because, for $\beta_{IV} \geq \beta^*_{IV}$, V_{ABC} monotonically decreases when deploying the triangle from w^i_A to w^c_A, so the compatible state corresponding to w^c_A can always be reached by deflation. To demonstrate the concept, in Fig. 2i, we consider 500,000 different geometries of Designs IV for which $\alpha^i_{xy} = \pi/4$, $\beta^i_{xy} \in [\pi/4 - \alpha_{IV}/2, \pi/2 - \alpha_{IV}]$ and $\beta_{IV} \in [\beta^i_{xy}, \pi/2[$, and find that all geometries with $\beta_{IV} \geq \beta^*_{IV}$ are inflatable. Furthermore, as β^*_{IV} is not affected by α^i_{xy} (see map of β^*_{IV} in Fig. 2h), an inflatable origami structure can be realized by assembling highly incompatible triangles lying near the upper bound of their design space. This results in inflatable designs with a maximum incompatibility, Δ^{max}, much higher than Designs I–III and with a flat stable state in the x–z plane (as for $\beta = \pi/2 - \alpha$ the compatible deployment height is such that the deployed triangle lies in the orthogonal x–z plane with $w^c_A = ||AC||$; see Supplementary Information section 1 for details). In full agreement with these findings, when we fabricate and test Design IV-D with $(\alpha_{IV\text{-}D}, \beta_{IV\text{-}D}) = (29^\circ, 56^\circ)$ and

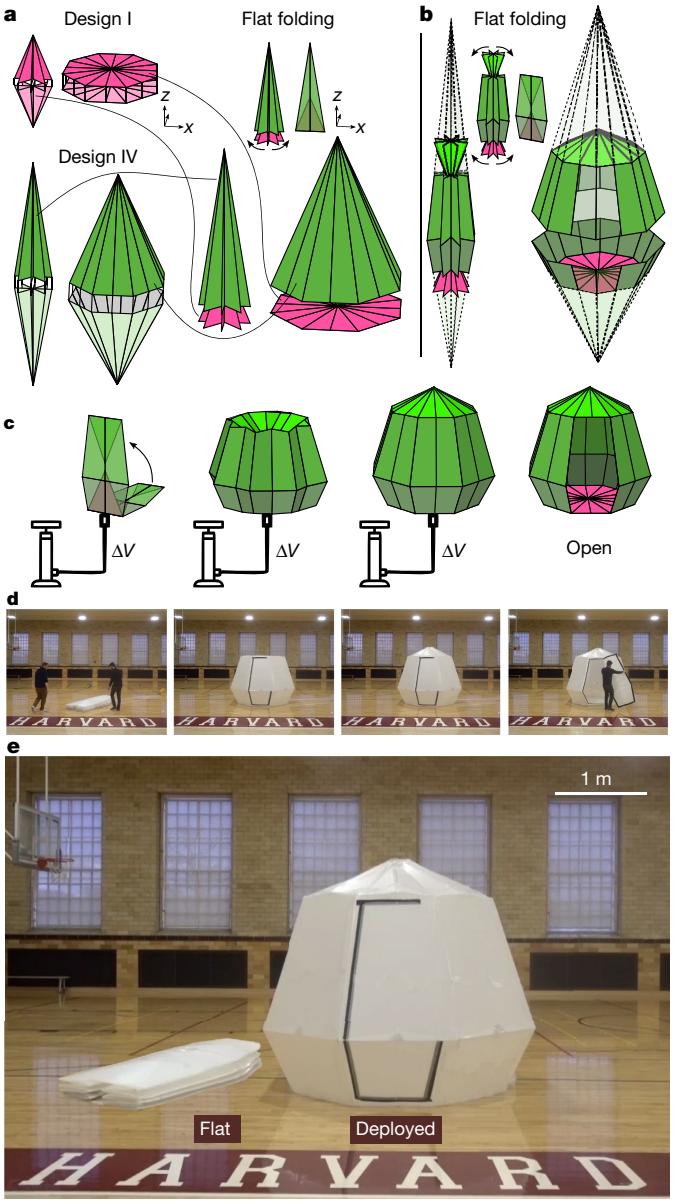

Fig. 4 | Metre-scale inflatable shelter. a, A tent-like design can be created by merging one layer of a Design I with another one of a Design IV. Note in that the initial, zero-volume configuration of the tent, both layers are in their compatible expanded state, whereas in the final inflated configuration of the tent, both layers are in their initial state (flat for Design I and initially rotated for Design IV). **b**, The initial volume can be further decreased by truncating the triangular facets into quadrilaterals and arranging successive layers of Design IV. **c**, Schematics illustrating the deployment process. **d**, The fabricated metre-scale inflatable shelter can be inflated from a compact state to a fully deployed state. Owing to multistability, the door can be opened, making the internal space accessible. **e**, Flat-folded and deployed state of the metre-scale inflatable shelter.

$(\alpha^i_{xy}, \beta^i_{xy}) = (45°, 33°)$ (for which $\Delta^{max}/||AB|| = 2.05 \times 10^{-1}$), we record the largest negative pressure and energy barrier in the deployed stable state (see green curve in Fig. 2j, Supplementary Video 2).

Metre-scale functional structures

As a next step, we use the simple geometries presented in Fig. 2 as a basis to design functional and easily deployable structures for real-world applications and build them at the metre scale.

First, we use the expanded wedge-like shapes of Designs III as building blocks to realize an inflatable archway. Focusing on Design III-C, we find that in the expanded stable state it has an opening angle $\theta_{III\text{-}C} = 40°$ (Fig. 3a). To design a deployable arch, we couple this unit with a different geometry of the same design family (which we referred to as Design III-C′) that (1) is bistable and deployable through inflation, (2) has an edge AB of equal length, (3) has an opening angle $\theta_{III\text{-}C'}$ such that when we alternate $m+1$ units of Design III-C′ with m units of Design III-C, we span an angle of 180° in the expanded configuration, and (4) has the larger triangle (referred to as triangle 1 in Fig. 2) identical to that of Design III-C but mirrored (that is, $\alpha^{(1)}_{III\text{-}C} = \beta^{(1)}_{III\text{-}C'}$ and $\beta^{(1)}_{III\text{-}C} = \alpha^{(1)}_{III\text{-}C'}$; Fig. 3b) to ensure compactness in the flat state. By inspecting the database of Fig. 2j, we find that for $m = 6$, all above requirements are satisfied when Design III-C′ is characterized by $(\alpha^{(1)}_{III\text{-}C'}, \beta^{(1)}_{III\text{-}C'}, \alpha^{(2)}_{III\text{-}C'}, \beta^{(2)}_{III\text{-}C'}) = (30°, 37°, 30°, 51°)$. However, as the resulting archway comprises 13 inflatable cavities, multiple pressure inputs would be needed to inflate it. To simplify the deployment process, we modify the structure by cutting it through the x–z mirror plane, separating the two resulting parts by a distance t, and connecting them with rectangular facets (see insets in Fig. 3c). As this procedure does not affect the geometric deployment of the triangles, we expect the additional facets to have a negligible impact on the structure's multistability, but to facilitate its inflatability by creating a single cavity. In Fig. 3d, we show a metre-scale version of this archway with $||AB|| = 30$ cm and $t = 10$ cm constructed out of corrugated plastic sheets (clear 8 ft × 4 ft, 4-mm-thick sheets). To build this structure, we use a digital cutting system to cut two parts (each comprising both triangular building blocks and rectangular facets; Supplementary Fig. 20) and pattern the hinges by scoring the sheets to locally reduce the thickness of the material. We then connect the two digitally cut parts using adhesive tape to form an airtight cavity (see Supplementary Information section 2 for details). In the folded configuration, the structure has a height of 20 cm and a width of 30 cm. Upon pressurization, it inflates into a 60-cm-tall and 150-cm-wide archway that, because of its multistability, preserves its shape even when the pressure is suddenly released (Supplementary Video 3). Finally, it can be folded back to the initial flat state by applying vacuum to overcome the energy barrier (Supplementary Video 3).

Another strategy to realize functional shapes is to merge components of different design families together to form a single cavity. As an example, we can create an inflatable tent-like geometry by combining one layer of a Design I with another one of a Design IV (Fig. 4a). To ensure successful merging, the two layers must have (1) outer edges BC of equal length, and (2) the same x–y projection in the two compatible states (that is, $\alpha^{(1)}_{I} = \alpha^{(2)}_{I} = \alpha^{i}_{xy}$ and $\beta^{(1)}_{I} = \beta^{(2)}_{I} = \beta^{i}_{xy}$). Furthermore, to realize structures with a fully flat compatible state, we choose the triangles to lie on the upper boundary of the deployable domain (that is, triangles with $\beta^{(1)}_{I} = \pi/2 - \alpha^{(1)}_{I}$ and $\beta^{(2)}_{I} = \pi/2 - \alpha^{(2)}_{I}$). By imposing these constraints, we can design tent-like structures that can be folded flat and expanded via inflation (see Supplementary Fig. 24 for a centimetre-scale version), but their compactness is limited by the long AB edge of the Design IV. To further decrease the occupied volume in the compact state, we truncate the triangular building blocks of the Design IV layer into quadrilaterals and add additional layers of Design IV, some of which can be folded inwardly. As shown in Fig. 4b, these operations not only reduce the initial volume but also result in a more liveable sheltered space in the deployed state. To demonstrate this strategy, we fabricate the structure shown in Fig. 4b at the metre scale, applying the same construction process used for the inflatable archway (see Supplementary Information section 2, Supplementary Video 4 for details). As shown in Fig. 4c, d, the structure can be folded completely flat (with the ceiling folded inward) to occupy a space of 1.0 × 2.0 × 0.25 m. When an input pressure is provided, the structure first expands to a stable configuration with the roof folded inward. Upon further pressurization, the roof snaps outwards and the final deployed shape of 2.5 × 2.6 × 2.6 m is reached. Importantly, because of the multistability, at this point the

door can be opened without impacting structural integrity, making the internal space accessible. Finally, using a vacuum, the shelter can be folded back to the flat configuration (Supplementary Video 3).

Conclusion

In summary, we have demonstrated how geometry can be efficiently exploited to realize pressure-deployable origami structures characterized by two stable configurations—one compact and one expanded. The design methodology presented in this work could be extended both to larger and smaller scales if properly accounting for loading conditions and fabrication challenges[4,10,11,20]. As our functional structures are multistable, they can also be designed to achieve target deployment sequences (Supplementary Fig. 25). In addition, by introducing building blocks comprising more than two different facets, we expect to further expand the range of achievable shapes (Supplementary Fig. 26). To that end, complementary to our geometric model and experiments, a mechanical model capable of predicting the full energy landscape[39,50] could provide a useful tool to guide such exploration. Finally, building on our results, deployable structures able to switch between targeted stable states could be efficiently identified by generalizing our design rules to arbitrary origami polyhedra and, combining them with stochastic optimization algorithms, solve the inverse design problem.

Online content

Any methods, additional references, Nature Research reporting summaries, source data, extended data, supplementary information, acknowledgements, peer review information; details of author contributions and competing interests; and statements of data and code availability are available at https://doi.org/10.1038/s41586-021-03407-4.

1. Pellegrino, S. *Deployable Structures in Engineering* (Springer-Verlag, 2014).
2. You, Z. & Pellegrino, S. Foldable bar structures. *Int. J. Solids Struct*. **34**, 1825–1847 (1997).
3. Liu, Y., Du, H., Liu, L. & Leng, J. Shape memory polymers and their composites in aerospace applications: a review. *Smart Mater. Struct*. **23**, 023001 (2014).
4. Puig, L., Barton, A. & Rando, N. A review on large deployable structures for astrophysics missions. *Acta Astron*. **67**, 12–26 (2010).
5. Zhao, J.-S., Chu, F. & Feng, Z.-J. The mechanism theory and application of deployable structures based on SLE. *Mech. Mach. Theory*, **44**, 324–335 (2009).
6. Mira, L. A., Thrall, A. P. & De Temmerman, N. Deployable scissor arch for transitional shelters. *Autom. Constr*. **43**, 123–131 (2014).
7. Thrall, A. P., Adriaenssens, S., Paya-Zaforteza, I. & Zoli, T. P. Linkage-based movable bridges: design methodology and three novel forms. *Eng. Struct*. **37**, 214–223 (2012).
8. Arnouts, L. I. W., Massart, T. J., De Temmerman, N. & Berke, P. Structural optimisation of a bistable deployable scissor module. In *Proc. IASS Annual Symposium 2019—Structural Membranes 2019* (eds Lázaro, C. et al.) (2019).
9. García-Mora, C. J. & Sánchez-Sánchez, J. Geometric method to design bistable and non—bistable deployable structures of straight scissors based on the convergence surface. *Mech. Mach. Theory* **146**, 103720 (2020).
10. Cadogan, D., Stein, J. & Grahne, M. Inflatable composite habitat structures for lunar and Mars exploration. *Acta Astron*. **44**, 399–406 (1999).
11. Block, J., Straubel, M. & Wiedemann, M. Ultralight deployable booms for solar sails and other large gossamer structures in space. *Acta Astron*. **68**, 984–992 (2011).
12. Sifert, E., Reyssat, E., Bico, J. & Roman, B. Programming stiff inflatable shells from planar patterned fabrics. *Soft Matter* **16**, 7898–7903 (2020).
13. Siéfert, E., Reyssat, E., Bico, J. & Roman, B. Bio-inspired pneumatic shape-morphing elastomers. *Nat. Mater*. **18**, 16692–16696 (2019).
14. Usevitch, N. S. et al. An untethered isoperimetric soft robot. *Sci. Robot*. **5**, eaaz0492 (2020).
15. Skouras, M. et al. Designing inflatable structures. *ACM Trans. Graph*. **33**, 63 (2014).
16. Rus, D. & Tolley, M. T. Design, fabrication and control of origami robots. *Nat. Rev. Mater*. **3**, 101–112 (2018).
17. Onal, C. D., Wood, R. J. & Rus, D. An origami-inspired approach to worm robots. *IEEE ASME Trans. Mechatron*. **18**, 430–438 (2013).
18. Onal, C. D., Tolley, M. T., Wood, R. J. & Rus, D. Origami-inspired printed robots. *IEEE ASME Trans. Mechatron*. **20**, 2214–2221 (2015).
19. Li, S. et al. A vacuum-driven origami "magic-ball" soft gripper. In *2019 International Conference on Robotics and Automation (ICRA)* 7401–7408 (IEEE, 2019).
20. Miskin, M. Z. et al. Graphene-based bimorphs for micron-sized, autonomous origami machines. *Proc. Natl Acad. Sci. USA* **115**, 466–470 (2018).
21. Silverberg, J. L. et al. Using origami design principles to fold reprogrammable mechanical metamaterials. *Science* **345**, 647–650 (2014).
22. Dudte, L. H., Vouga, E., Tachi, T. & Mahadevan, L. Programming curvature using origami tessellations. *Nat. Mater*. **15**, 583–588 (2016).
23. Filipov, E. T., Tachi, T. & Paulino, G. H. Origami tubes assembled into stiff, yet reconfigurable structures and metamaterials. *Proc. Natl Acad. Sci. USA* **112**, 12321–12326 (2015).
24. Overvelde, J. T. B., Weaver, J. C., Hoberman, C. & Bertoldi, K. Rational design of reconfigurable prismatic architected materials. *Nature* **541**, 347–352 (2017).
25. Iniguez-Rabago, A., Li, Y. & Overvelde, J. T. B. Exploring multistability in prismatic metamaterials through local actuation. *Nat. Commun*. **10**, 5577 (2019).
26. Seymour, K. et al. Origami-based deployable ballistic barrier. In *Proc. 7th International Meeting on Origami in Science Mathematics and Education* 763–778 (2018).
27. Del Grosso, A. & Basso, P. Adaptive building skin structures. *Smart Mater. Struct*. **19**, 124011 (2010).
28. Tachi, T. in *Origami 5* (eds Wang-Iverson, P. et al.) Ch. 20 (CRC Press, 2011).
29. Zirbel, S. A. et al. Accommodating thickness in origami-based deployable arrays. *J. Mech. Des*. **135**, 111005 (2013).
30. You, Z. & Cole, N. Self-locking bi-stable deployable booms. In *47th AIAA/ASME/ASCE/AHS/ASC Structures, Structural Dynamics, and Materials Conference* AIAA 2006-1685 (ARC, 2006); https://arc.aiaa.org/doi/abs/10.2514/6.2006-1685.
31. Lang., R. J. A computational algorithm for origami design. In *Proc. 12th Annual ACM Symposium on Computational Geometry* 98–105 (1996); https://ci.nii.ac.jp/naid/80009084712/en/.
32. Demaine, E. D. & Mitchell, J. S. B. Reaching folded states of a rectangular piece of paper. In *Proc. 13th Canadian Conference on Computational Geometry (CCCG 2001)* 73–75 (2001).
33. Demaine, E. D. & Tachi, T. Origamizer: a practical algorithm for folding any polyhedron. In *Proc. 33rd International Symposium on Computational Geometry (SoCG 2017)* **34**:1–34:15 (2017).
34. Martinez, R. V., Fish, C. R., Chen, X. & Whitesides, G. M. Elastomeric origami: programmable paper-elastomer composites as pneumatic actuators. *Adv. Funct. Mater*. **22**, 1376–1384 (2012).
35. Li, S., Vogt, D. M., Rus, D. & Wood, R. J. Fluid-driven origami-inspired artificial muscles. *Proc. Natl Acad. Sci. USA* **114**, 13132–13137 (2017).
36. Kim, W. et al. Bioinspired dual-morphing stretchable origami. *Sci. Robot*. **4**, eaay3493 (2019).
37. Kamrava, S., Mousanezhad, D., Ebrahimi, H., Ghosh, R. & Vaziri, A. Origami-based cellular metamaterial with auxetic, bistable, and self-locking properties. *Sci. Rep*. **7**, 46046 (2017).
38. Hanna, B., Lund, J., Lang, R., Magleby, S. & Howell, L. Waterbomb base: a symmetric single-vertex bistable origami mechanism. *Smart Mater. Struct*. **23**, 094009 (2014).
39. Cai, J., Deng, X., Ya, Z., Jian, F. & Tu, Y. Bistable behavior of the cylindrical origami structure with Kresling pattern. *J. Mech. Des*. **137**, 061406 (2015).
40. Silverberg, J. L. et al. Origami structures with a critical transition to bistability arising from hidden degrees of freedom. *Nat. Mater*. **14**, 389–393 (2015).
41. Waitukaitis, S., Menaut, R., Gin-ge Chen, B. & van Hecke, M. Origami multistability: from single vertices to metasheets. *Phys. Rev. Lett*. **114**, 055503 (2015).
42. Yasuda, H. & Yang, J. Reentrant origami-based metamaterials with negative Poisson's ratio and bistability. *Phys. Rev. Lett*. **114**, 185502 (2015).
43. Reid, A., Lechenault, F., Rica, S. & Adda-Bedia, M. Geometry and design of origami bellows with tunable response. *Phys. Rev. E* **95**, 013002 (2017).
44. Faber, J. A., Arrieta, A. F. & Studart, A. R. Bioinspired spring origami. *Science* **359**, 1386–1391 (2018).
45. Dolciani, M. P., Donnelly, A. J. & Jurgensen, R. C. *Modern Geometry, Structure and Method* (Houghton Mifflin, 1963).
46. Connelly, R. The rigidity of polyhedral surfaces. *Math. Mag*. **52**, 275–283 (1979).
47. Connelly, R., Sabitov, I. & Walz, A. The bellows conjecture. *Contrib. Algebr. Geom*. **38**, 1–10 (1997).
48. Mackenzie, D. Polyhedra can bend but not breathe. *Science* **279**, 1637–1637 (1998).
49. Chen, Y., Feng, H., Ma, J., Peng, R. & You, Z. Symmetric waterbomb origami. *Proc. R. Soc. A* **472**, 20150846 (2016).
50. Paulino, G. H. & Liu. K. Nonlinear mechanics of non-rigid origami: an efficient computational approach. *Proc. R. Soc. A* **473**, 20170348 (2017).

Methods

The details of the design, materials and fabrication methods are summarized in Supplementary Information sections 1, 2. The experimental procedure of the inflation with water to measure the pressure–volume curve is described in Supplementary Information section 3. Finally, additional information about extending our methodology to more complex designs is provided in Supplementary Information section 4.

Data availability

The datasets generated or analysed during the current study are available from the corresponding author on reasonable request.

Code availability

The code generated during the current study is available from the corresponding author on reasonable request.

Acknowledgements We thank E. Demaine, J. Ku, T. Tachi and Yunfang Yang for insightful discussions; S. Lindner-Liaw, M. Bhattacharya and M. Starkey for assistance in the fabrication of the centimetre-scale and large-scale structures; and A. E. Forte for his valuable comments and suggestions on the manuscript. This research was supported by NSF through the Harvard University Materials Research Science and Engineering Center grant number DMR-1420570 and DMREF grant number DMR-1922321, as well as the Fund for Scientific Research-Flanders (FWO).

Author contributions D.M., B.G., C.H. and K.B. proposed and developed the research idea. D.M. conducted the numerical calculations. D.M., B.G. and C.J.G.-M. designed and fabricated the centimetre-scale and metre-scale structures. D.M. performed the experiments. D.M., B.G. and K.B. wrote the paper. K.B. supervised the research.

Competing interests The authors declare no competing interests.

Additional information

Supplementary information The online version contains supplementary material available at https://doi.org/10.1038/s41586-021-03407-4.

Correspondence and requests for materials should be addressed to C.H. or K.B.

Peer review information *Nature* thanks Larry Howell, Glaucio Paulino and the other, anonymous, reviewer(s) for their contribution to the peer review of this work. Peer reviewer reports are available.

nature portfolio

https://doi.org/10.1038/s41586-021-03407-4

Supplementary information

Multistable inflatable origami structures at the metre scale

In the format provided by the authors and unedited

Supplementary Materials

Multistable inflatable origami structures at the meter-scale

David Melancon, Benjamin Gorissen, Carlos J. García-Mora, Chuck Hoberman, and Katia Bertoldi

E-mail: bertoldi@seas.harvard.edu

This PDF file includes:

Figs. S1 to S30
Captions for Videos S1 to S4

Other supplementary materials for this manuscript include the following:

Videos S1 to S4

S1. Design

Our origami-inspired deployable structures are made out of stiff triangular facets connected by compliant hinges. In this Section, we first show that the inscribed angle theorem can be utilized to design triangular building blocks with two compatible states. Next, we demonstrate that assembling these building blocks in rational ways leads to a library of inflatable and bistable origami shapes.

Deployment of an initially flat triangular building block. We start by considering a triangular building block ABC with internal angle $\alpha \equiv \angle BAC$ and $\beta \equiv \angle ABC$. The triangle is initially flat (i.e. it lies in the xy-plane) and is deployed through a rotation about its edge BC, which leads to a displacement w_A of vertex A along the z-direction and a volume under the triangle, V_{ABC}, that can be calculated as

$$V_{ABC} = \frac{1}{6} AB \cdot (AC \times AA_{xy}) = \frac{w_A ||AB||^2}{6} \frac{\sin\alpha}{\sin(\alpha+\beta)} \sqrt{\sin^2\beta - \frac{w_A^2}{||AB||^2}}, \quad [1]$$

where AA_{xy} is the segment formed by connecting vertex A to its projection on the xy-plane, $||AB||$ is the length of edge AB, and $w_A = ||AA_{xy}||$ (see Fig. S1a). Focusing on the xy-plane (see Figs. S1b–c), we see that, if

$$\alpha \in]\alpha_{min}, \alpha_{max}[= \left]0, \frac{\pi}{2}\right[, \quad \text{and} \quad \beta \in [\beta_{min}, \beta_{max}] = \left[\frac{\pi}{4} - \frac{\alpha}{2}, \frac{\pi}{2} - \alpha\right], \quad [2]$$

the projection of the triangle intersects a circle circumscribed to the initial configuration at a displacement, w_A^c, and volume, V_{ABC}^c. The displacement w_A^c can be obtained as

$$w_A^c = \sqrt{||AC||^2 - ||AC_{xy}^c||^2} = ||AB|| \sqrt{1 - \frac{\cos^2\beta}{\sin^2(\alpha+\beta)}}, \quad [3]$$

where $||AC||$ is the length of edge AC and AC_{xy}^c is the edge AC projected on the xy-plane at the intersection with the circle, whose length is given by

$$||AC_{xy}^c|| = ||AB|| \cot(\alpha+\beta). \quad [4]$$

Further, by substituting Eq. (3) in Eq. (1), we get

$$V_{ABC}^c = \frac{||AB||^3}{6} \sin\alpha \sin\beta \cos\beta \csc(\alpha+\beta) \cot(\alpha+\beta) \sqrt{1 - \cot^2\beta \cot^2(\alpha+\beta)}. \quad [5]$$

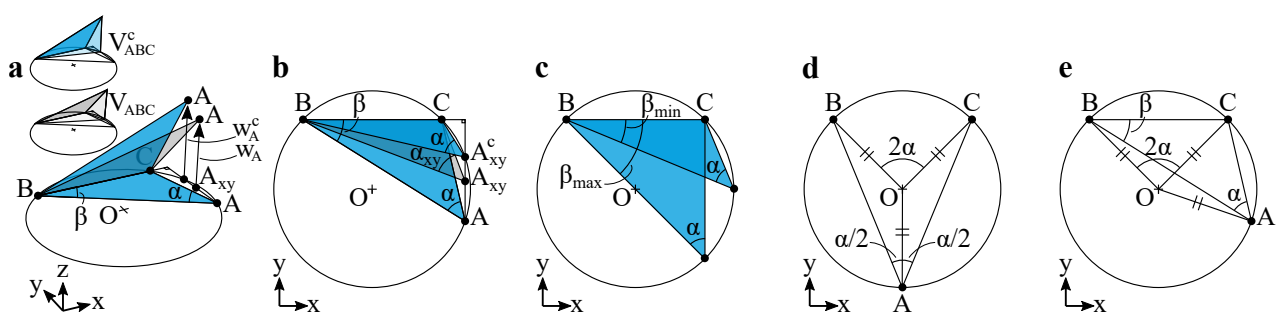

Fig. S1. Deployment of an initially flat triangular building block. (a-b). Isometric and projected views of a triangular building block ABC that recovers its projected angle α during deployment leading to two distinct compatible states. **(c).** Initially flat triangular building block ABC in the limit cases where $\beta = \beta_{min}$ and $\beta = \beta_{max}$. **(d).** According to the inscribed angle theorem, the angle $\angle BAC$ is half the central angle $\angle BOC$. **(e).** Moving the vertex A on the circle below the edge BC does not change the angle $\angle BAC$.

It follows from the inscribed angle theorem (which states that, since the angle α inscribed in a circle is half of the central angle that subtends the same arc, α does not change as its vertex is moved on the circle—see Figs. S1d-e) that for $w_A = w_A^c$ and $V_{ABC} = V_{ABC}^c$, the angle α is recovered on the projected plane. As such, the triangle ABC possesses two states—one flat and one deployed—for which $\alpha = \alpha_{xy}$ separated by states for which $\alpha_{xy} \neq \alpha$ (see gray triangle is Figs. S1a-b). Using simple geometry, we can determine α_{xy} as a function of w_A as

$$\alpha_{xy} = \arccos\left(\frac{AB_{xy} \cdot AC_{xy}}{||AB_{xy}|| \cdot ||AC_{xy}||}\right) = \arccos\left(\frac{1 - 2\frac{w_A^2}{||AB||^2} - \frac{\sin(\alpha-\beta)}{\sin(\alpha+\beta)}}{2\sqrt{1 - \frac{w_A^2}{||AB||^2}}\sqrt{\left(\frac{\sin\beta}{\sin(\alpha+\beta)}\right)^2 - \frac{w_A^2}{||AB||^2}}}\right), \quad [6]$$

where AB_{xy} and AC_{xy} are the edges AB and AC projected on the xy-plane, which have length

$$||AB_{xy}|| = \sqrt{1 - \frac{w_A^2}{||AB||^2}}, \qquad [7]$$

and

$$||AC_{xy}|| = ||AB|| \sqrt{\frac{\sin^2\beta}{\sin^2(\alpha+\beta)} - \frac{w_A^2}{||AB||^2}}. \qquad [8]$$

In Fig. S2a, we show the evolution of the projected angle variation, i.e. $\Delta\alpha \equiv \alpha_{xy} - \alpha$, as a function of w_A for a triangular building block with $\alpha = 45°$ and $\beta = 32°$. We find a highly non-linear relation characterized by a local maximum

$$\Delta\alpha_{max} \equiv \max(\Delta\alpha) = \arccos\left(\frac{2\cot(\alpha+\beta)\sin 2\beta}{\sqrt{\csc^4(\alpha+\beta)\sin 2\beta \sin(2(\alpha+\beta))\sin^2(\alpha+2\beta)}}\right), \qquad [9]$$

at a deployment height

$$w_A^{\Delta\alpha_{max}} = ||AB|| \sin\beta \sqrt{1 - \cot\beta\cot(\alpha+\beta)}. \qquad [10]$$

and two points ($w_A = 0$ and $w_A = w_A^c$) at which $\Delta\alpha = 0$.

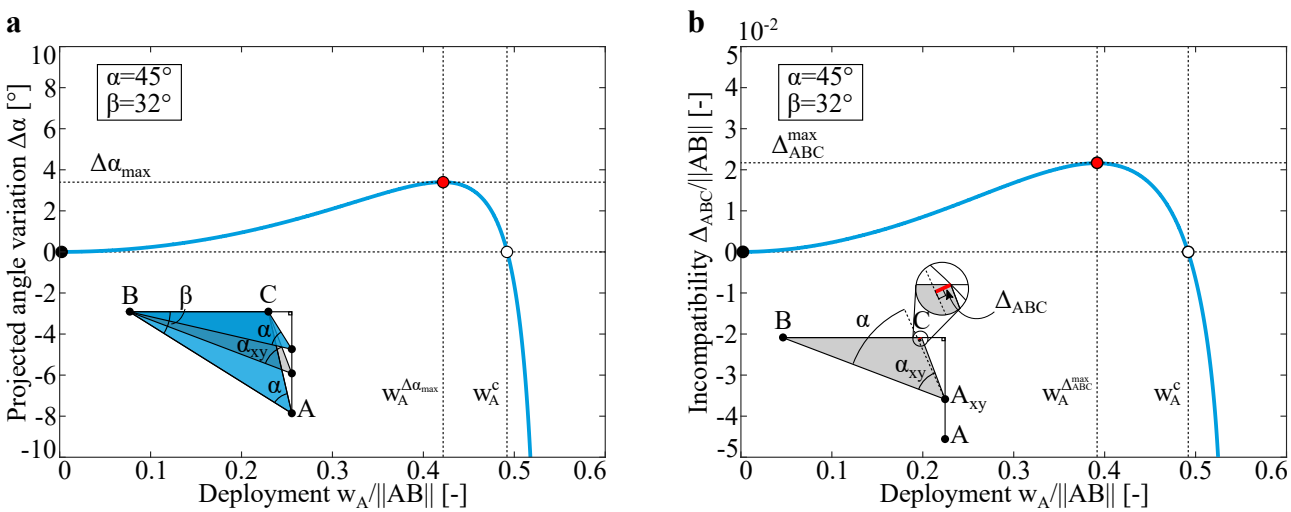

Fig. S2. Evolution of $\Delta\alpha$ and Δ_{ABC} during deployment. (a-b). Evolution of $\Delta\alpha$ and Δ_{ABC} as a function of the deployment of vertex A, w_A, for a triangle with $\alpha = 45°$ and $\beta = 32°$.

Further, the difference between α_{xy} and α can also be quantified by introducing the distance

$$\Delta_{ABC} = ||AC_{xy}|| \cdot \sin\Delta\alpha = ||AC_{xy}|| \cdot \sin(\alpha_{xy} - \alpha), \qquad [11]$$

that we will later use to characterize the geometric incompatibility of the resulting origami structures for $0 < w_A < w_A^c$ and, therefore, estimate the energy required for them to snap back from the expanded to the flat state. In Fig. S2b, we show the evolution of Δ_{ABC} as a function of w_A for a triangle with $\alpha = 45°$ and $\beta = 32°$. As expected, we find a similar behavior to that reported in Fig. S2a for $\Delta\alpha$, with a local maximum $\Delta_{ABC}^{max} \equiv \max(\Delta_{ABC})$ at a deployed height $w_A^{\Delta_{ABC}^{max}}$ and two points ($w_A = 0$ and w_A^c) at which $\Delta_{ABC} = 0$.

Next, in Fig. S3 we show the effect of α and β on Δ_{ABC}. First, in Fig. S3a we investigate how β affects the Δ_{ABC} vs. w_A curve when choosing $\alpha = 45°$. We find that

- for $\beta \to \beta_{min} = \pi/4 - \alpha/2$

$$w_A^c \to 0, \quad \text{and} \quad \Delta_{ABC}^{max} = \max(\Delta_{ABC}) \to 0. \qquad [12]$$

- for $\beta \to \beta_{max} = \pi/2 - \alpha$, Δ_{ABC}^{max} largely increases and

$$w_A^c \to w_A^{\Delta_{ABC}^{max}}. \qquad [13]$$

As shown in Fig. S3b, similar trends are found when increasing the angle α for a fixed value of β (here we choose $\beta = 45°$). It is also interesting to note that for $\alpha = 60°$ Δ_{ABC} monotonically increases and the triangle does not have a deployed compatible state. This is because for $\alpha = 60°$, $\beta = 45° > \beta_{max} = \pi/2 - \alpha$.

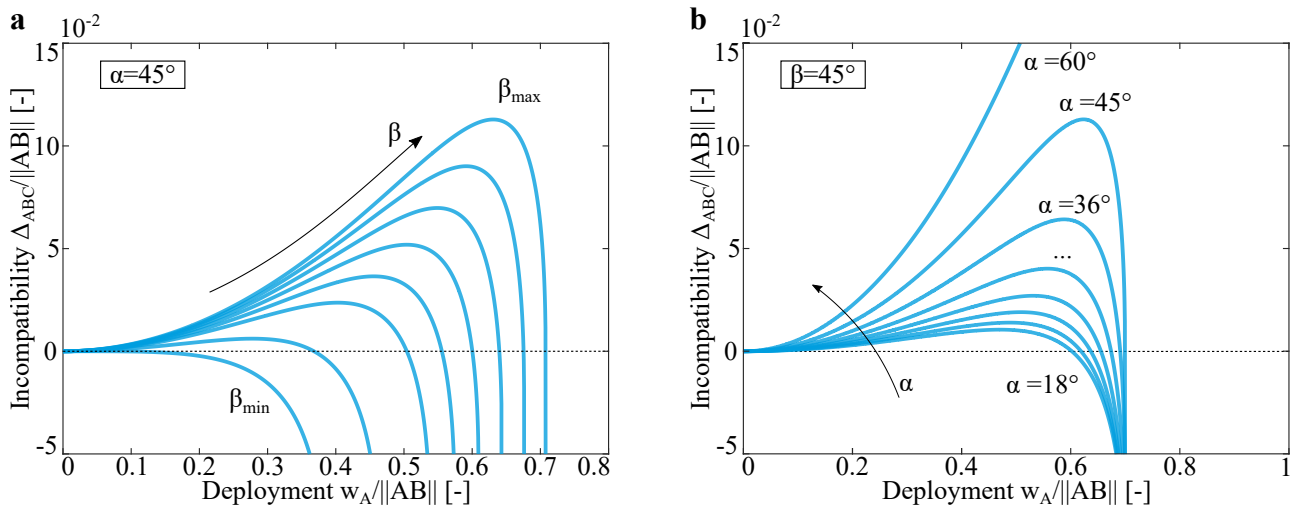

Fig. S3. Effect of α and β on the Δ_{ABC}-w_A curve. (a). Effect of varying β for triangles with $\alpha = 45°$. **(b)**. Effect of varying α for triangles with $\beta = 45°$.

To identify triangles that can potentially lead to deployable structures that are inflatable, we then plot the evolution of Δ_{ABC} as a function of V_{ABC}. In Fig. S4a we report such curves for triangles with $\alpha = 45°$ and $\beta \in [22.5°, 45°]$ and highlight two important volume configurations: the volume at the deployed compatible state , V^c_{ABC} (white circular marker), and the maximum volume, V^{max}_{ABC} (green circular marker), that can be expressed as

$$V^{max}_{ABC} = \frac{||AB||^3}{12} \frac{\sin\alpha \sin^2\beta}{\sin(\alpha+\beta)}. \qquad [14]$$

We find that for low values of β the deployed compatible state with corresponding volume, V^c_{ABC}, is reached before the state of maximum volume, V^{max}_{ABC}, enabling actuation through inflation (see inset on the lower left corner of Fig. S4a). Differently, for large values of β the configuration of maximum volume is reached before the deployed compatible state and, therefore, that state cannot be reached through inflation (see inset on the upper left corner of Fig. S4a). Note that these trends are also found when considering a triangle with $\beta = 27°$ and $\alpha \in [36°, 60°]$ (see Fig. S4b). Guided by these results, we then introduce the inflation constraint

$$h_{ABC} = \frac{\Gamma^{V^{max}_{ABC}}}{\Gamma^c}, \qquad [15]$$

where $\Gamma^{V^{max}_{ABC}}$ and Γ^c are the arc lengths measured on the Δ_{ABC}-V_{ABC} curve between the flat compatible state and the state of maximum volume and between the flat and expanded compatible configurations, respectively (see Fig. S4a). It follows from Eq. (15) that only triangles with $\log h_{ABC} \geq 0$ can be deployed through fluidic actuation as those are the only ones for which the expanded compatible configuration is reached before the one with maximum volume during inflation.
Finally, in Fig. S5 we summarize the results derived here by reporting contour maps of the compatible deployment height, w^c_A, the compatible deployment volume, V^c_{ABC}, the maximum volume, V^{max}_{ABC}, the maximum geometric incompatibility, Δ^{max}_{ABC}, and the inflation constraint, $\log h_{ABC}$.

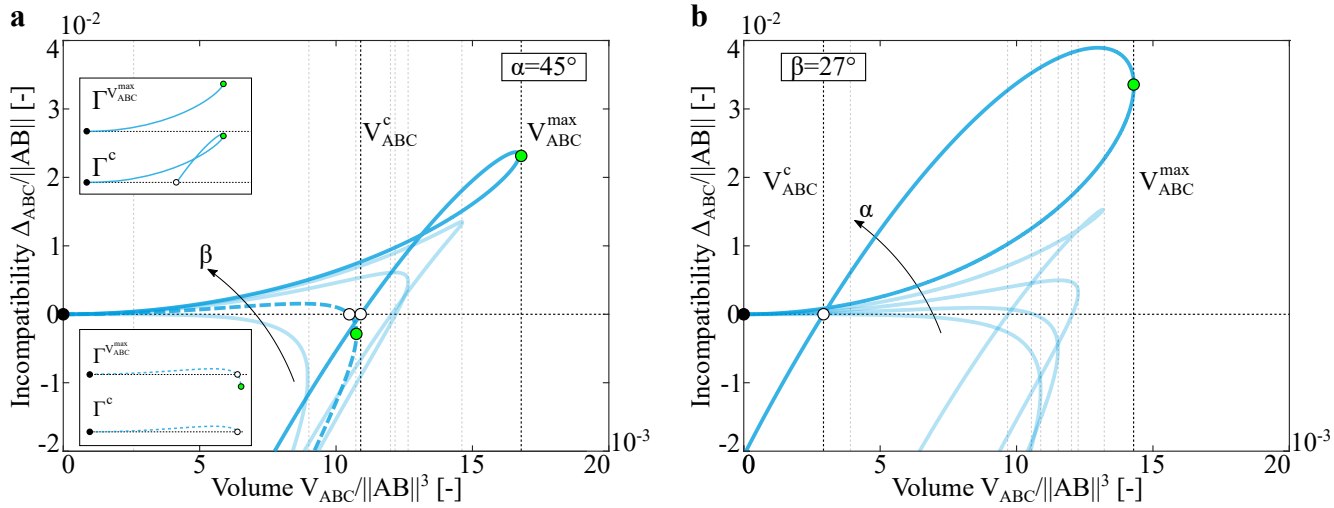

Fig. S4. Effect of α and β on the Δ_{ABC}-V_{ABC} curve. (a). Effect of varying β for triangles with $\alpha = 45°$. The compatible, V^c_{ABC}, and maximum, V^{max}_{ABC}, volume states are highlighted for $\beta = 45°$.**(b)**. Effect of varying α for triangles with $\beta = 27°$. The compatible, V^c_{ABC}, and maximum, V^{max}_{ABC}, volume states are highlighted for $\alpha = 60°$.

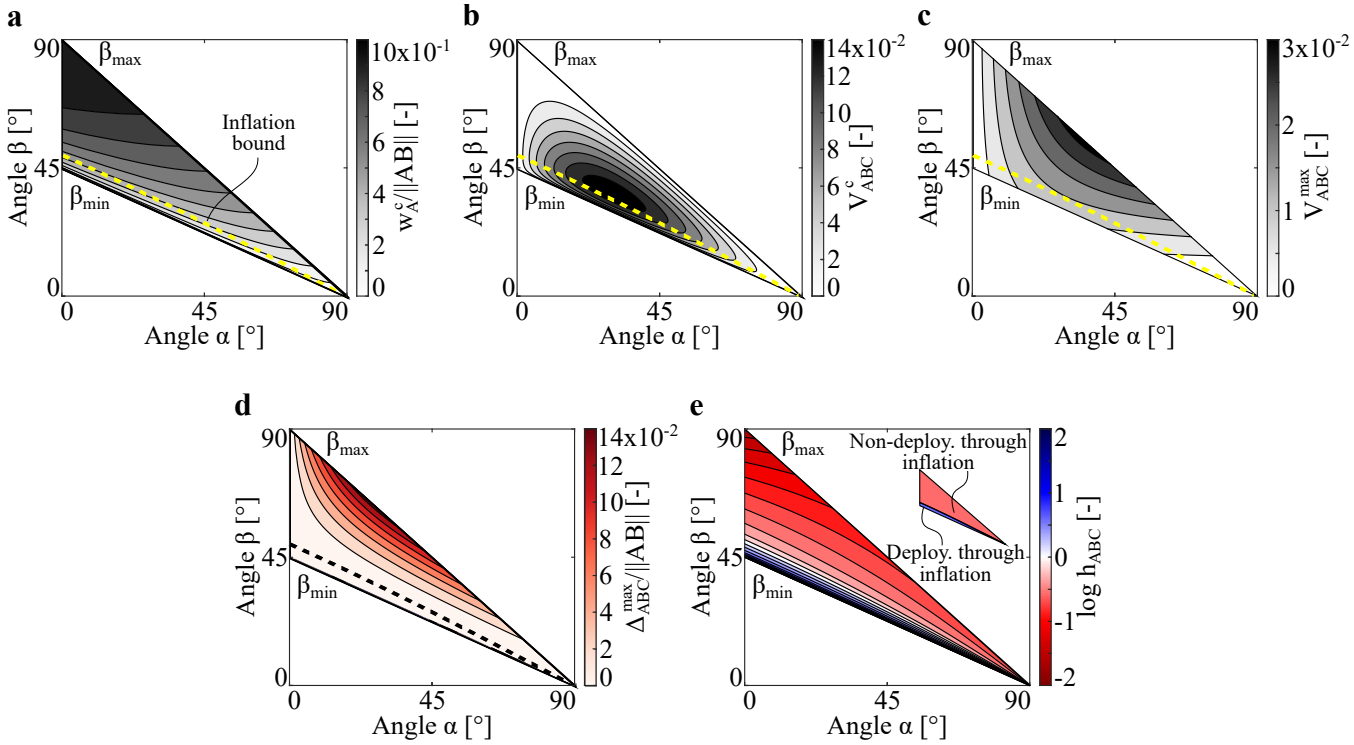

Fig. S5. Deployment of an initially flat triangular building block: summary of derived results. (a-e). Contour maps of (a) the compatible deployment height, w^c_A, (b) the volume at the deployed compatible state, V^c_{ABC}, (c) the maximum volume, V^{max}_{ABC}, (d) the maximum incompatibility during deployment, Δ^{max}_{ABC}, and (e) the inflation constraint, $\log h_{ABC}$, as a function of the angles α and β.

Deployment of an initially rotated triangular building block. So far, we have focused on triangular building blocks defined by internal angles α and β that initially lie in the xy-plane and recover their projected angle α in a deployed state on such plane for $w_A = w_A^c$ and $V_{ABC} = V_{ABC}^c$. However, the triangle in the xy-plane can also be seen as the projection of a triangle with internal angles α and β that has been initially rotated around its edge BC to have a deployment height w_A^i, volume under the triangle V_{ABC}^i, and projected angles α_{xy}^i and β_{xy}^i (see Fig. S6). Note that such initially rotated building block is fully defined by the projected angles α_{xy}^i and β_{xy}^i and the internal angle β and that its other geometric parameters, α and w_A^i, can be derived from simple geometric considerations as

$$\alpha = \pi - \arccos\left(\frac{\sqrt{2}\left(\cos 2\,\beta - \frac{\sin\left(\alpha_{xy}^i + 2\,\beta_{xy}^i\right)}{\sin\alpha_{xy}^i}\right)}{\sqrt{-\frac{\frac{\cos 2\,\alpha_{xy}^i + \cos\left(2\,\alpha_{xy}^i + 4\,\beta_{xy}^i\right) - 2}{\sin\alpha_{xy}^i} + 4\,\cos 2\,\beta\,\sin\left(\alpha_{xy}^i + 2\,\beta_{xy}^i\right)}{\sin\alpha_{xy}^i}}}\right), \qquad [16]$$

and

$$w_A^i = \sqrt{||AC||^2 - ||AC_{xy}^i||^2} = ||AB||\sin\beta\sqrt{1 - \frac{\tan^2\beta_{xy}^i}{\tan^2\beta}}, \qquad [17]$$

where AC_{xy}^i is the edge AC projected on the xy-plane at the first intersection with the circle, whose length is given by

$$||AC_{xy}^i|| = ||AB||\frac{\cos\beta\tan\beta_{xy}^i}{\sin(\alpha_{xy}^i + \beta_{xy}^i)}. \qquad [18]$$

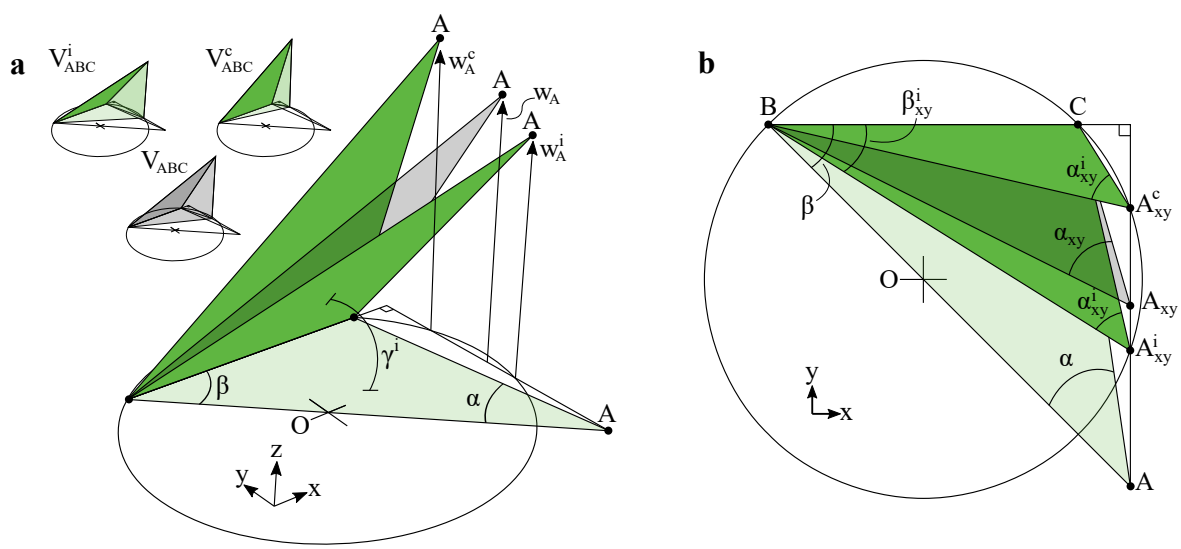

Fig. S6. Deployment of an initially rotated triangular building block. (a-b). Isometric and projected views of a triangular building block ABC that recovers its projected angle α_{xy}^i during deployment leading to two distinct compatible states.

Further, by substituting Eq. (17) into Eq. (1), we find that the volume initially under the triangle is

$$V_{ABC}^i = \frac{||AB||^3}{6}\frac{\cos^2\beta\,\sin\alpha_{xy}^i\,\sin\beta\,\tan\beta_{xy}^i}{\sin\left(\alpha_{xy}^i + \beta_{xy}^i\right)\cos\beta_{xy}^i}\sqrt{1 - \frac{\tan^2\beta_{xy}^i}{\tan^2\beta}}. \qquad [19]$$

Focusing on the xy-plane (see Fig. S6b), we see that, if

$$\begin{aligned} \alpha_{xy}^i &\in \left]\left(\alpha_{xy}^i\right)_{min}, \left(\alpha_{xy}^i\right)_{max}\right[= \left]0, \frac{\pi}{2}\right[, \\ \beta_{xy}^i &\in \left[\left(\beta_{xy}^i\right)_{min}, \left(\beta_{xy}^i\right)_{max}\right] = \left[\frac{\pi}{4} - \frac{\alpha_{xy}^i}{2}, \frac{\pi}{2} - \alpha_{xy}^i\right], \\ \beta &\in [\beta_{min}, \beta_{max}[= \left[\beta_{xy}^i, \frac{\pi}{2}\right[, \end{aligned} \qquad [20]$$

upon further rotation the projection of the triangle intersects a circle circumscribed to the initial configuration also at a displacement, w_A^c, and volume, V_{ABC}^c. The displacement w_A^c can be obtained as

$$w_A^c = \sqrt{||AC||^2 - ||AC_{xy}^c||^2} = ||AB|| \sin\beta \sqrt{1 - \cot^2(\alpha_{xy}^i + \beta_{xy}^i)\cot^2\beta}, \quad [21]$$

where AC_{xy}^c is the edge AC projected on the xy-plane at the second intersection with the circle, whose length is given by

$$||AC_{xy}^c|| = ||AB|| \frac{\cos\beta \cot\left(\alpha_{xy}^i + \beta_{xy}^i\right)}{\cos\beta_{xy}^i}. \quad [22]$$

Further, by substituting Eq. (21) in Eq. (1), we get

$$V_{ABC}^c = \frac{||AB||^3}{6} \frac{\cos^2\beta \, \sin(\alpha_{xy}^i) \, \sin\beta}{\sin\left(\alpha_{xy}^i + \beta_{xy}^i\right) \tan\left(\alpha_{xy}^i + \beta_{xy}^i\right) \cos\left(\beta_{xy}^i\right)} \sqrt{1 - \cot^2\left(\alpha_{xy}^i + \beta_{xy}^i\right)\cot^2\beta} \quad [23]$$

It follows from the inscribed angle theorem that for $w_A = w_A^c$ and $V_{ABC} = V_{ABC}^c$, the projected angle α_{xy}^i is recovered on the projected plane. As such, the triangle ABC possesses two states – identified by w_A^i and w_A^c – for which $\alpha_{xy}^i = \alpha_{xy}$ separated by states for which $\alpha_{xy}^i \neq \alpha_{xy}$, where α_{xy} is still given by Eq. (6).

In Fig. S7a we show the evolution of the projected angle variation, $\Delta\alpha \equiv \alpha_{xy} - \alpha_{xy}^i$, as a function of w_A for a triangular building block with $\beta = 45°$, $\alpha_{xy}^i = 45°$, and $\beta_{xy}^i = 32°$ (for which $\alpha = 36.8°$ according to Eq. (16)). We find a non-linear relationship similar to that obtained for the initially flat building blocks, characterized by a local maximum

$$\Delta\alpha_{max} \equiv \max(\Delta\alpha) = \arccos\left(\frac{2\cot(\alpha_{xy}^i + \beta_{xy}^i)\sin 2\beta_{xy}^i}{\sqrt{\csc^4(\alpha_{xy}^i + \beta_{xy}^i)\sin 2\beta_{xy}^i \sin(2(\alpha_{xy}^i + \beta_{xy}^i))\sin^2(\alpha_{xy}^i + 2\beta_{xy}^i)}}\right), \quad [24]$$

at

$$w_A^{\Delta\alpha_{max}} = ||AB|| \sin\beta \sqrt{1 - \tan\beta_{xy}^i \cot^2\beta \cot(\alpha_{xy}^i + \beta_{xy}^i)}. \quad [25]$$

and two points ($w_A = w_A^i$ and $w_A = w_A^c$) at which $\Delta\alpha = 0$.

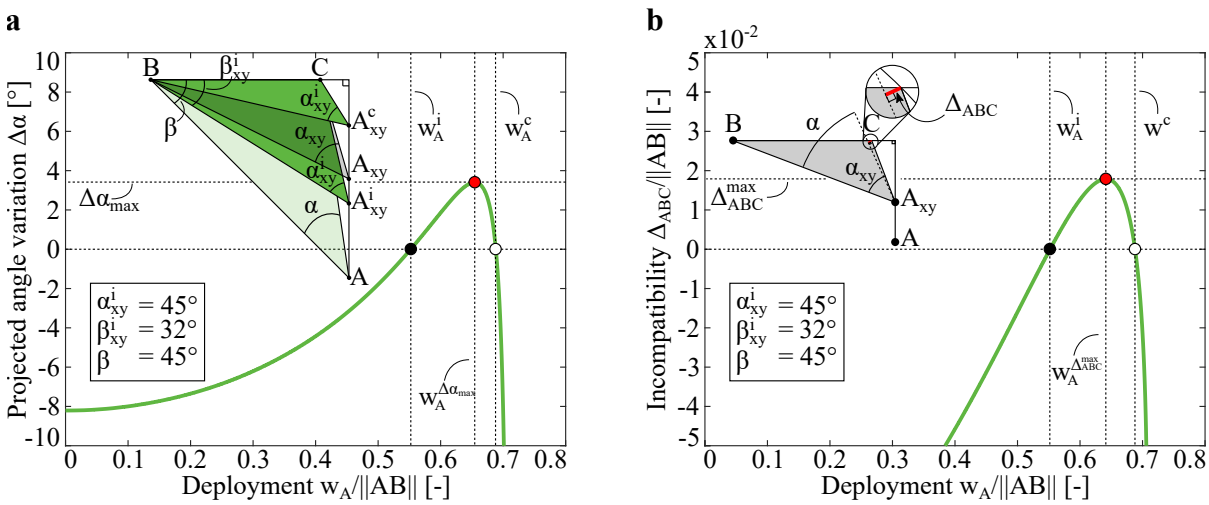

Fig. S7. Evolution of $\Delta\alpha$ and Δ_{ABC} during deployment. (a-b). Evolution of (a) $\Delta\alpha$ and (b) Δ_{ABC} as a function of the deployment of vertex A, w_A, for a triangle with $\alpha_{xy}^i = 45°$, $\beta_{xy}^i = 32°$ and $\beta = 45°$. The red circular marker indicates the local maximum, whereas the black and white circular markers indicate the two compatible configurations.

As for the initially flat building blocks, also in this case we can quantify the difference between α_{xy} and α_{xy}^i by introducing the distance

$$\Delta_{ABC} = ||AC_{xy}|| \cdot \sin(\alpha_{xy} - \alpha_{xy}^i), \quad [26]$$

where $||AC_{xy}||$ is given in Eq. (8). In Fig. S7b we show the evolution of Δ_{ABC} as a function of w_A for a triangular building block with $\beta = 45°$, $\alpha_{xy}^i = 45°$, and $\beta_{xy}^i = 32°$. Again, we find a behavior similar to that observed for the initially flat building blocks, with a local maximum $\Delta_{ABC}^{max} \equiv \max(\Delta_{ABC})$ at $w_A^{\Delta_{ABC}^{max}}$ and two points ($w_A = w_A^i$ and w_A^c) at which $\Delta_{ABC} = 0$.

Next, in Fig. S8 we explore the effect of α_{xy}^i, β_{xy}^i, and β on Δ_{ABC}. First, in Fig. S8a we investigate how β_{xy}^i affects the Δ_{ABC} vs. w_A curve when choosing $\alpha_{xy}^i = 45°$ and $\beta = 45°$. We find that

- for $\beta_{xy}^i \to \left(\beta_{xy}^i\right)_{min} = \pi/4 - \alpha_{xy}^i/2$

$$w_A^i \to w_A^c, \quad \text{and} \quad \Delta_{ABC}^{max} = \max\left(\Delta_{ABC}\right) \to 0. \quad [27]$$

- for $\beta^i_{xy} \to \left(\beta^i_{xy}\right)_{max} = \pi/2 - \alpha^i_{xy}$, Δ^{max}_{ABC} largely increases and

$$w^i_A \to 0, \quad \text{and} \quad w^c_A \to w_A^{\Delta^{max}_{ABC}}. \tag{28}$$

As shown in Fig. S8b, we find similar trends when increasing the angle α_{xy}, while keeping $\beta^i_{xy} = 32°$ and $\beta = 45°$. However, as expected from Eq. (17), in this case the initial deployment height, w^i_A, is constant and not affected by α^i_{xy}. Finally, in Fig. S8c we investigate how β affects the Δ_{ABC} vs. w_A curve for triangles with $\alpha^i_{xy} = 45°$ and $\beta^i_{xy} = 45°$. By varying β over the range $[\beta^i_{xy}, \pi/2[$, we find that

- for $\beta \to \beta^i_{xy}$ we recover the case of the initially flat triangular building block and

$$w^i_A \to 0 \tag{29}$$

- for $\beta \to \pi/2$, Δ^{max}_{ABC} slightly decreases and

$$w^i_A \to w^c_A. \tag{30}$$

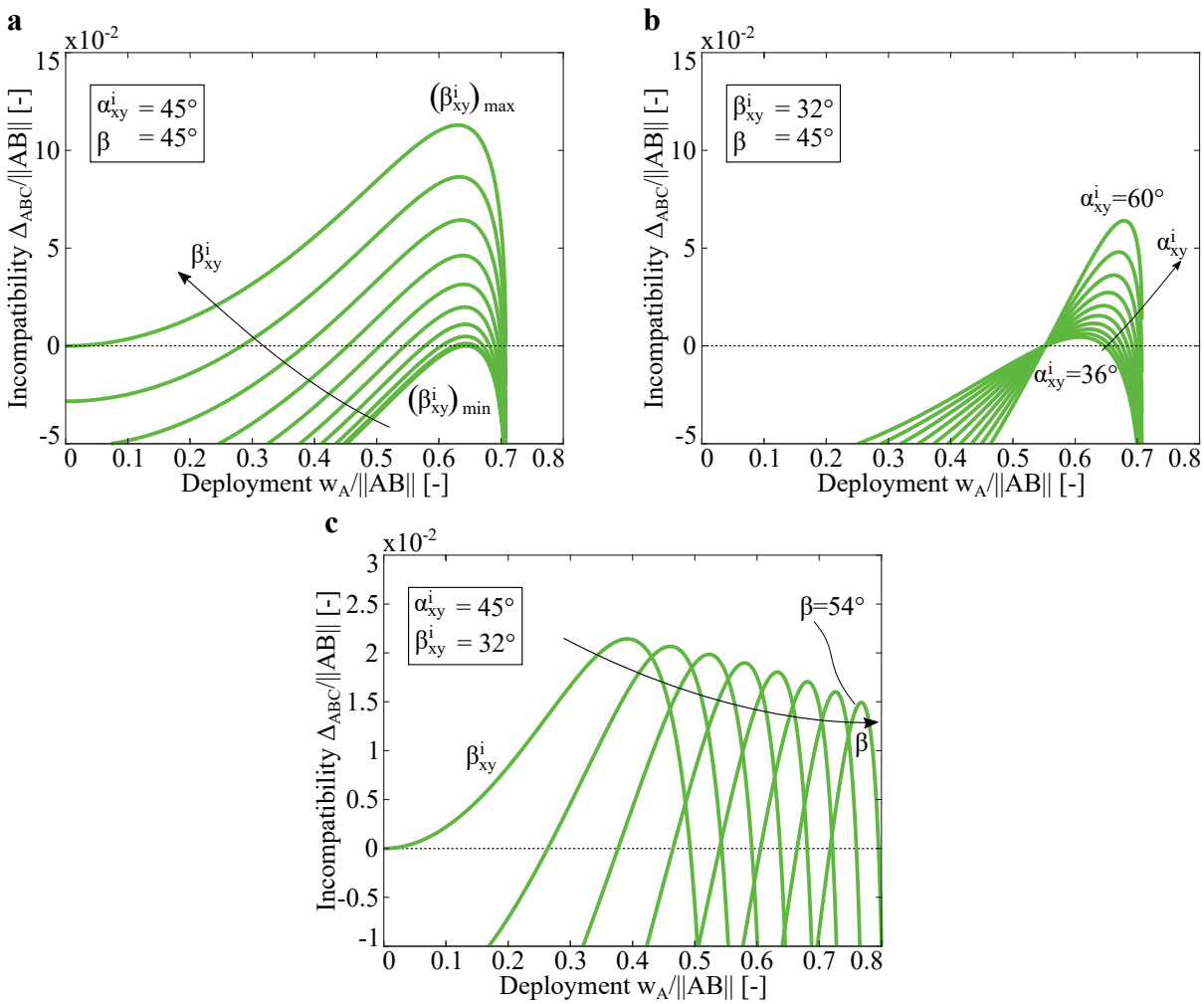

Fig. S8. Effect of β, α^i_{xy}, and β^i_{xy} on the Δ_{ABC}-w_A curve. (a). Effect of varying β^i_{xy} for triangles with $\alpha^i_{xy} = 45°$ and $\beta = 45°$. **(b)**. Effect of varying α^i_{xy} for triangles with $\beta^i_{xy} = 32°$ and $\beta = 45°$. **(c)**. Effect of varying β for triangles with $\alpha^i_{xy} = 45°$ and $\beta^i_{xy} = 32°$.

To identify triangles that can potentially lead to deployable structures that are inflatable, we then plot the evolution of Δ_{ABC} as a function of V_{ABC}. In Fig. S9a we report such curves for triangles with $\alpha^i_{xy} = 45°$, $\beta = 45°$ and $\beta^i_{xy} \in [22.5°, 45°]$ and highlight two important volume configurations: the volume at the deployed compatible state , V^c_{ABC} (white circular marker), and the maximum volume, V^{max}_{ABC} (green circular marker), that can be calculated from Eq. (14). We find that for low values of β^i_{xy}, both deployed compatible state with corresponding volumes, V^i_{ABC} and V^c_{ABC} are reached before the state of maximum volume V^{max}_{ABC}, enabling actuation through inflation (see green dashed line in Fig. S9a). Differently, for large values of β the configuration of maximum volume is reached before the deployed compatible state with corresponding volume V^i_{ABC} and, therefore, that state cannot be reached through inflation (see green solid line in Fig. S9a). Note that similar trends are also found when considering a triangle with $\beta^i_{xy} = 32°$ and $\beta = 45°$ and $\alpha^i_{xy} \in [36°, 60°]$ (see Fig. S9b), although the effect of increasing α^i_{xy} is substantially smaller than β_{xy} on inflatability.

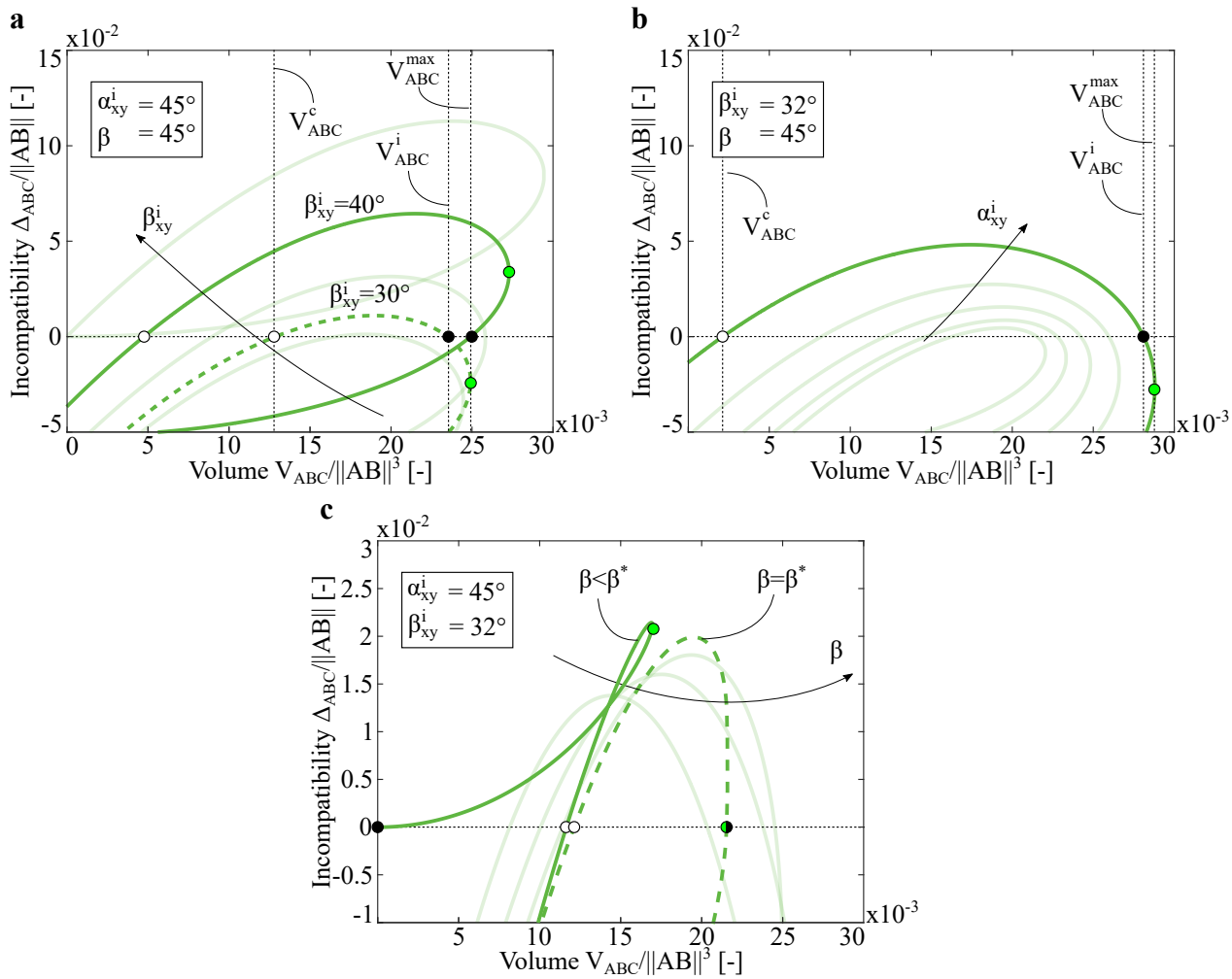

Fig. S9. Effect of β, α^i_{xy}, and β^i_{xy} on the Δ_{ABC}-V_{ABC} curve. (a). Effect of varying β^i_{xy} for triangles with $\alpha^i_{xy} = 45°$ and $\beta = 45°$. **(b).** Effect of varying α^i_{xy} for triangles with $\beta^i_{xy} = 32°$ and $\beta = 45°$. **(c).** Effect of varying β for triangles with $\alpha^i_{xy} = 45°$ and $\beta^i_{xy} = 32°$.

To identify initially rotated triangles that can deployed through fluidic actuation, we then use the inflation constraint defined in Eq. (15). An interesting feature of the initially rotated building block is that for any combination of α^i_{xy} and β^i_{xy} (within the bounds defined in Eq. (20)), we can always select β such that $\log h_{ABC} \geq 0$. This is because we can set $\beta = \beta^*$, where β^* is the angle resulting in an initial rotated state defined by the deployment w^i_A that maximizes the volume under the triangle, i.e. $V^i_{ABC} = V^{max}_{ABC}$ (see Fig. S9c where for $\beta = \beta^*$ the black and green markers coincide). To determine β^*, we first determine the deployment angle, γ_i, by finding the dihedral angle (see Fig. S6a) between the planes of the flat and deployed triangles ABC

$$\gamma_i = \arccos\left(\frac{n_0 \cdot n_{w^i_A}}{||n_0|| \cdot ||n_{w^i_A}||}\right) = \arccos\left(\sqrt{\left(1 - \frac{w_A^2}{||AB||^2 \sin^2\beta}\right)}\right), \qquad [31]$$

where n_0 and n_{w_A} are the normals of the planes defined by the flat and deployed triangles. Noting that a triangle maximizes its volume when the deployment angle is $\gamma_i = \pi/4$ and replacing w_A in Eq. (31) by the expression of w^i_A in Eq. (17), we find

$$\beta^* = \tan^{-1}\left(\sqrt{2}\tan\beta^i_{xy}\right). \quad [32]$$

Importantly, we expect an origami structure made out of initially rotated triangles with $\beta \geq \beta^*$ to be bistable and inflatable even if made out of a single building block.

Finally, in Fig. S10 we summarize the results derived here by reporting contour maps of the maximum geometric incompatibility, Δ^{max}_{ABC}, the inflation constraint, $\log h_{ABC}$, the compatible deployment heights, w^i_A and w^c_A, the compatible deployment volumes, V^i_{ABC} and V^c_{ABC}, and the maximum volume, V^{max}_{ABC} for three different values of β, i.e. $\beta = 30^\circ$, 45°, and 60°.

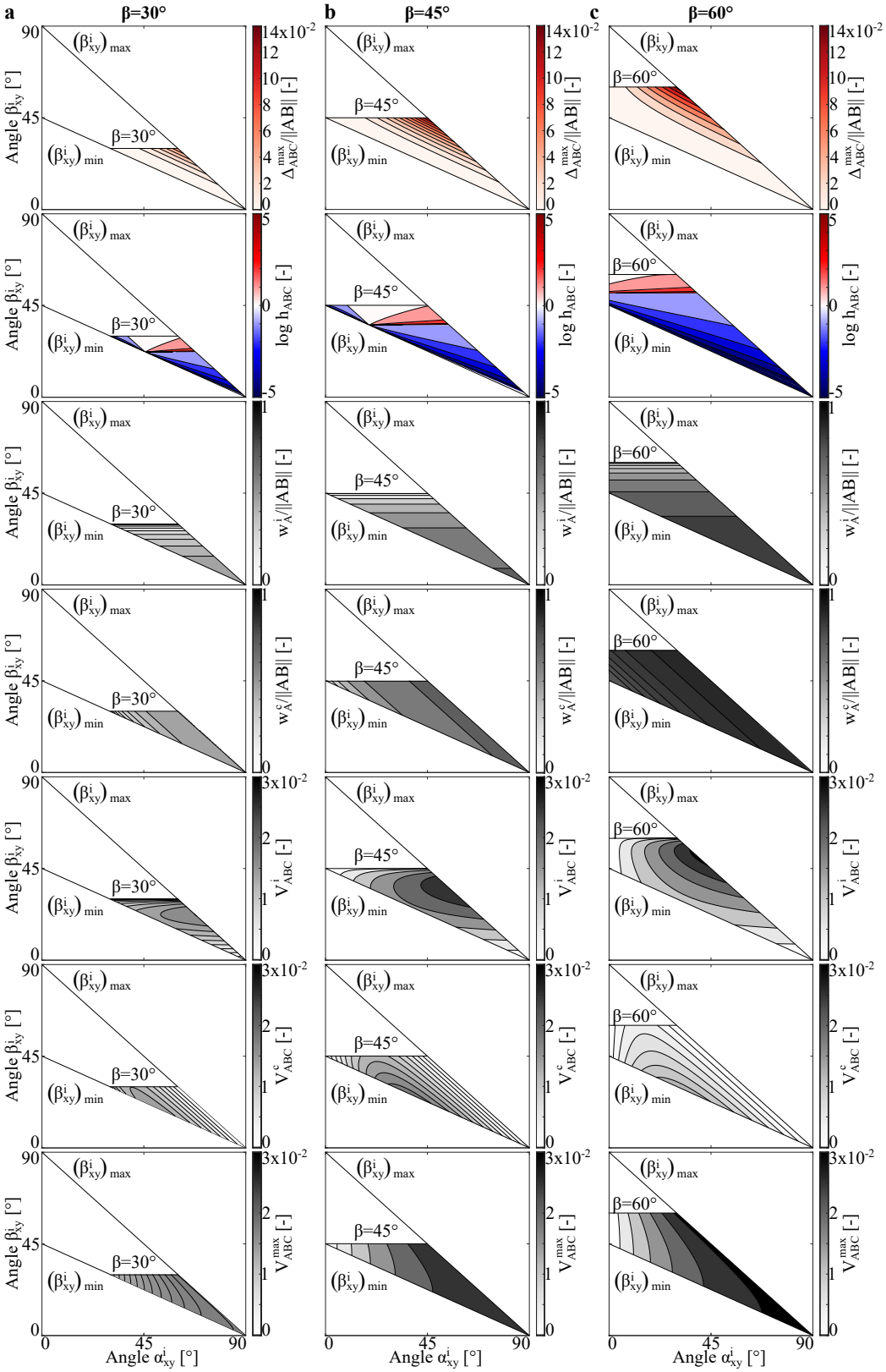

Fig. S10. Deployment of an initially rotated triangular building block: summary of derived results. (a-c). Contour maps of the maximum geometric incompatibility, Δ^{max}_{ABC}, the inflation constraint, $\log h_{ABC}$, the compatible deployment heights, w^i_A and w^c_A, the compatible deployment volumes, V^i_{ABC} and V^c_{ABC}, and the maximum volume, V^{max}_{ABC} for three different values of β, i.e. (a) $\beta = 30°$, (b) $45°$, and (c) $60°$.

Inflatable and bistable origami shapes. To realize inflatable origami structures with multiple stable states, we assemble the triangular building blocks discussed above. In this work, we present four different ways of connecting the building blocks to obtain a library of origami shapes. For three of them (which will be referred to as Designs I, Designs II, and Designs III) we utilize initially flat building blocks, whereas for the fourth one (which will be referred to as Design IV) we utilize initially rotated building blocks.

Designs I. To realize Designs I, we arrange $2n$ initially flat triangles with angles $(\alpha^{(1)}, \beta^{(1)})$ with $2n$ initially flat triangles with angles $(\alpha^{(2)}, \beta^{(2)})$ to form two identical layers with n-fold symmetry and connect them at their outer boundaries (see Fig. S11). The resulting star-like structures define an internal volume

$$V = 2n(V^{(1)}_{ABC} + V^{(2)}_{ABC}), \tag{33}$$

exhibit geometric incompatibility

$$\Delta = 2n(\Delta^{(1)}_{ABC} + \Delta^{(2)}_{ABC}) \tag{34}$$

and are inflatable only if

$$\log h = \log\left(\frac{\Gamma^{V^{max}}}{\Gamma^{c}}\right) \geq 0, \tag{35}$$

where $\Gamma^{V^{max}}$ and Γ^{c} are the arc lengths measured on the Δ-V curve between the states with $V = 0$ and $V = V^{max} = \max(V)$ and between the two stable configurations, respectively. Note that to ensure structural integrity, the two triangular building blocks must have

(i) identical compatible deployment heights, i.e. $w^{c(1)}_{A} = w^{c(2)}_{A}$;

(ii) connecting deployed edges AB of equal length, i.e $||AB^{(1)}|| = ||AB^{(2)}||$;

(iii) angles that satisfy $\alpha^{(1)} + \alpha^{(2)} = \pi/n$.

Therefore, to realize a Design I structure, we first select the number of symmetric folds, n, and the angles of the first triangular building blocks $\alpha^{(1)}$ and $\beta^{(1)}$. It follows from requirements (i-iii) that the second triangular building block must have its internal angles equal to

$$\begin{aligned} \alpha^{(2)} &= \pi/n - \alpha^{(1)}, \\ \beta^{(2)} &= \arctan\left(\frac{\sin(\alpha^{(1)} + \beta^{(1)})}{\cos\beta^{(1)}\cos\alpha^{(2)}} - \tan\alpha^{(2)}\right). \end{aligned} \tag{36}$$

In Figs. S11a-c, we show an example of a Design I geometry (referred to as Design I-A), with $(\alpha^{(1)}_{\text{I-A}}, \beta^{(1)}_{\text{I-A}}) = (22°, 35°)$ and $(\alpha^{(2)}_{\text{I-A}}, \beta^{(2)}_{\text{I-A}}) = (68°, 14°)$ for which $\Delta^{max}/||AB|| = 2.67 \times 10^{-2}$ and $\log h = 0$. Finally, in Fig. S11d, we plot the evolution of the maximum incompatibility, $\Delta^{max} \equiv \max(\Delta)$, as a function of the inflation constraint, $\log h$, for 500,000 different geometries with $n \in [2, 5]$, $\alpha \in]0, \pi/n[$, and $\beta \in [\pi/4 - \alpha/2, \pi/2 - \alpha]$ (note that the increase in brightness of the data points in Fig. S11d indicates an increase in number of symmetry folds, n, of the origami geometry).

Designs II. With the goal of increasing the geometric incompatibility of the inflatable designs, we investigate the response of star-like structures in which the longest edge of one triangle, $AB^{(1)}$, is connected to the shortest edge of the other one, $AC^{(2)}$. These geometries must satisfy the same requirements (i-iii) as Design I, except that we impose $||AB^{(1)}|| = ||AC^{(2)}||$ instead of $||AB^{(1)}|| = ||AB^{(2)}||$. Also in this case, to realize a Design II structure, we first select the number of symmetric folds, n, and the angles of the first triangular building block $\alpha^{(1)}$ and $\beta^{(1)}$. It then follows from requirements (i-iii) that the second triangular building block must have its internal angles equal to

$$\begin{aligned} \alpha^{(2)} &= \pi/n - \alpha^{(1)}, \\ \beta^{(2)} &= \arctan\left(\frac{\sin\beta^{(1)}}{\cos(\alpha^{(1)} + \beta^{(1)})\cos\alpha^{(2)}} - \tan\alpha^{(2)}\right). \end{aligned} \tag{37}$$

In Figs. S12a-c, we show an example of a Design II geometry (referred to as Design II-B), with $(\alpha^{(1)}_{\text{II-B}}, \beta^{(1)}_{\text{II-B}}) = (43.6°, 25.2°)$ and $(\alpha^{(2)}_{\text{II-B}}, \beta^{(2)}_{\text{II-B}}) = (46.4°, 33.5°)$ for which $\Delta^{max}/||AB|| = 8.58 \times 10^{-2}$ and $\log h = 0$. Finally, in Fig. S12d, we plot the evolution of the maximum incompatibility, Δ^{max}, as a function of the inflation constraint, $\log h$, for 500,000 different geometries with $n \in [2, 5]$, $\alpha \in]0, \pi/n[$, and $\beta \in [\pi/4 - \alpha/2, \pi/2 - \alpha]$.

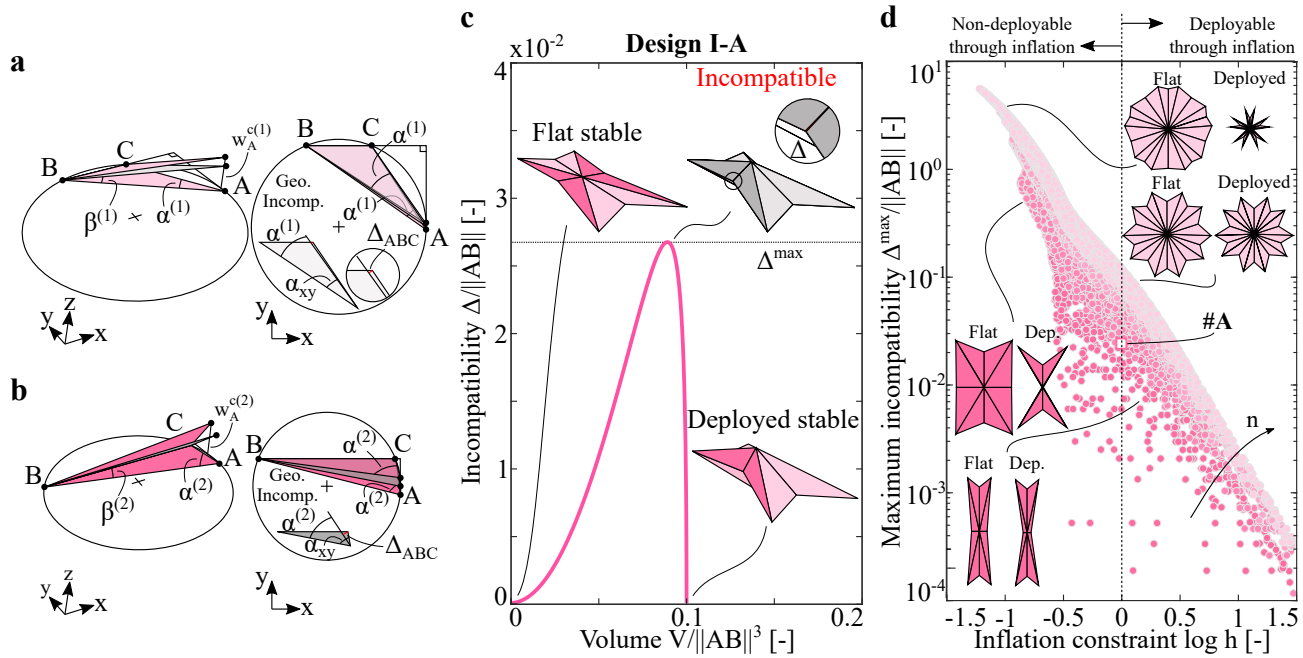

Fig. S11. Designs I. (a-b). Isometric and projected views of the two building blocks used to create Design I-A. **(c)**. Evolution of the incompatibility, Δ, as a function of the internal volume, V, for Design I-A. **(d)**. Maximum incompatibility, Δ^{max} vs. inflation constraint, $\log h$ for $500,000$ different Designs I geometries for increasing value of symmetry fold, n.

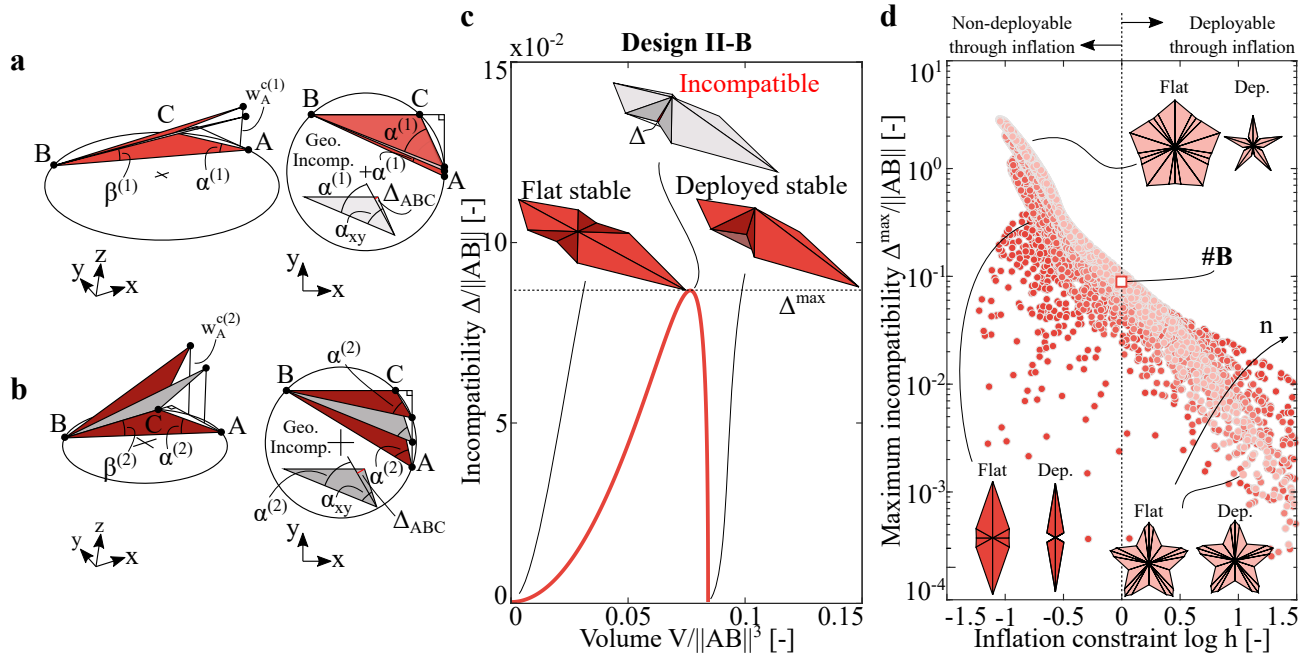

Fig. S12. Designs II. (a-b). Isometric and projected views of the two building blocks used to create Design II-B. **(c)**. Evolution of the incompatibility, Δ, as a function of the internal volume, V, for Design II-B. **(d)**. Maximum incompatibility, Δ^{max} vs. inflation constraint, $\log h$ for $500,000$ different Designs II geometries for increasing value of symmetry fold, n.

Designs III. Whereas the connection of two different initially flat triangles side by side enables us to design inflatable and bistable structures, it limits us to star-like shapes. To expand the range of shapes, we next arrange the two triangles on top of each other in the flat configuration and mirror them twice to form an inflatable cavity (see Fig. S13). This leads to geometries comprising eight triangles that are initially flat and transformed into wedge-like shapes upon deployment. These geometries define an internal volume

$$V = 4\left(V^{(1)}_{ABC} - V^{(2)}_{ABC}\right), \tag{38}$$

exhibit geometric incompatibility

$$\Delta = 4\left(\Delta^{(1)}_{ABC} + \Delta^{(2)}_{ABC}\right) \tag{39}$$

and are inflatable only if the constraint given in Eq. (35) is satisfied. Note that to ensure structural integrity, the two triangular building blocks must have

(i) identical compatible deployment heights, i.e. $w_A^{c(1)} = w_A^{c(2)}$;

(ii) connecting deployed edges of equal length, i.e $||AB^{(1)}|| = ||AC^{(2)}||$;

(iii) angles that satisfy $\alpha^{(1)} = \alpha^{(2)}$.

Therefore, to realize a Design III structure, we first select the angle of the first triangular building block $\alpha^{(1)}$ and $\beta^{(1)}$. It then follows from requirements (i-iii) that the second triangular building blocks must have its internal angles equal to

$$\begin{aligned} \alpha^{(2)} &= \alpha^{(1)}, \\ \beta^{(2)} &= \arctan\left(\frac{\sin\beta^{(1)}}{\cos(\alpha^{(1)}+\beta^{(1)})\cos\alpha^{(2)}} - \tan\alpha^{(2)}\right). \end{aligned} \tag{40}$$

In Figs. S13a-c, we show an example of a Design III geometry (referred to as Design III-C), with $(\alpha^{(1)}_{\text{III-C}}, \beta^{(1)}_{\text{III-C}}) = (37.1°, 30.0°)$ and $(\alpha^{(2)}_{\text{III-C}}, \beta^{(2)}_{\text{III-C}}) = (37.1°, 40.6°)$ for which $\Delta^{max}/||AB|| = 9.93 \times 10^{-2}$ and $\log h = 0.544$. Finally, in Fig. S13d, we plot the evolution of the maximum incompatibility, Δ^{max}, as a function of the inflation constraint, $\log h$, for $500,000$ different geometries with $\alpha \in]0, \pi/2[$, and $\beta \in [\pi/4 - \alpha/2, \pi/2 - \alpha]$.

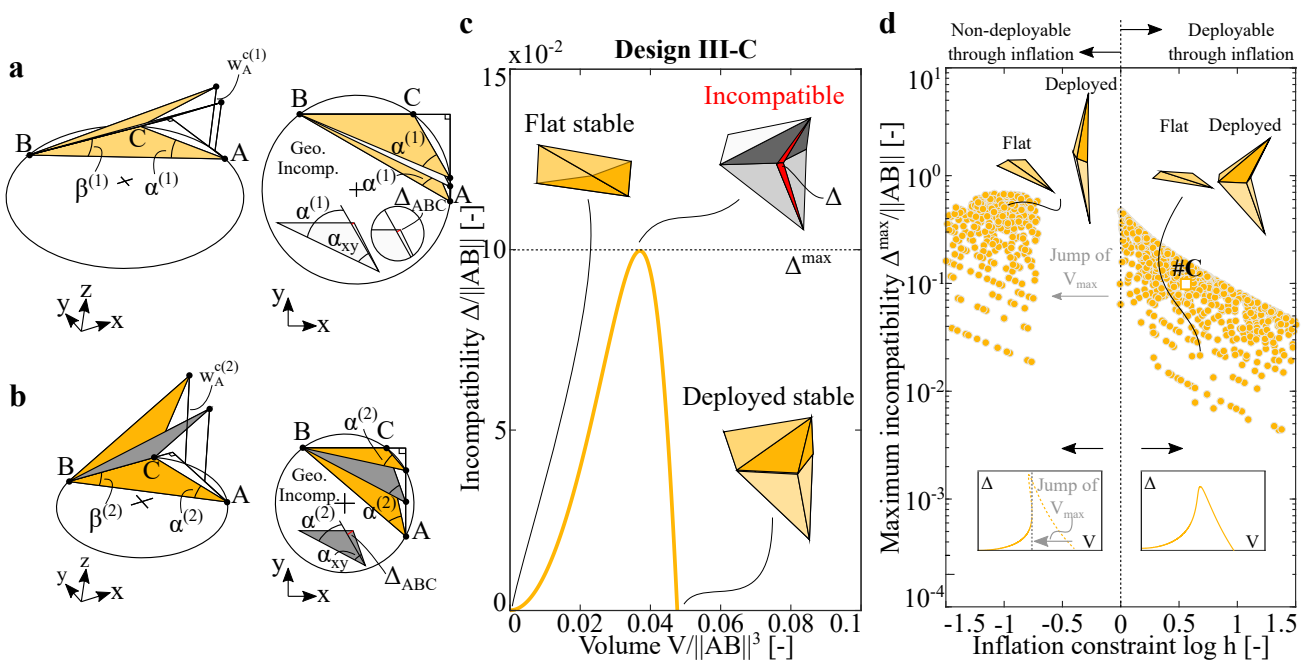

Fig. S13. Designs III. (a-b). Isometric and projected views of the two building blocks used to create Design III-C. **(c)**. Evolution of the incompatibility, Δ, as a function of the internal volume, V, for Design III-C. **(d)**. Maximum incompatibility, Δ^{max} vs. inflation constraint, $\log h$ for $500,000$ different Designs III geometries.

Designs IV. To realize Designs IV, we arrange $4n$ initially deployed triangles with angles α and β to form two identical layers with n-fold symmetry and connect them at their outer boundaries (see Fig. S14). Note that in this case, since we can choose $\beta > \beta^*$, we can use only one triangular building block to make bistable and inflatable structures. The resulting star-like structures define an internal volume

$$V = 4nV_{ABC}, \tag{41}$$

exhibit geometric incompatibility

$$\Delta = 4n\Delta_{ABC}, \qquad [42]$$

and are inflatable only if

$$\log h = \log\left(\frac{\Gamma^{V^{max}}}{\Gamma^{c}}\right) \geq 0, \qquad [43]$$

where $\Gamma^{V^{max}}$ and Γ^c are the arc lengths measured on the Δ-V curve between the states with $V = 4nV^i_{ABC}$ and $V = V^{max} = \max(V)$ and between the two stable configurations, respectively. Note that to ensure structural integrity, the triangular building blocks must have

(i) projected angle $\alpha^i_{xy} = \pi/n$;

(ii) projected angle $\beta^i_{xy} \in [\pi/4 - \alpha^i_{xy}/2, \pi/2 - \alpha^i_{xy}]$;

(iii) interior angle $\beta \in [\beta^i_{xy}, \pi/2[$.

Therefore, to realize a Design IV structure, we first select the number of symmetric folds, n, the projected angle β^i_{xy} and the interior angle β. Then, we use Eq. (16) to determine α. Note that to make the structure deployable through inflation (i.e. $\log h \geq 0$) we have to select $\beta \geq \beta^*$.

In Figs. S14a-c, we show an example of a Design IV geometry (referred to as Design IV-D), with $(\alpha_{\text{IV-D}}, \beta_{\text{IV-D}}) = (29°, 56°)$ and $(\alpha^i_{xy}, \beta^i_{xy}) = (45°, 33°)$ for which $\Delta^{max}/||AB|| = 2.05 \times 10^{-1}$ and $\log h = 0.508$. Finally, in Fig. S14d, we plot the evolution of the maximum incompatibility, Δ^{max}, as a function of the inflation constraint, $\log h$, for $500,000$ different geometries with $n \in [3, 5]$, $\beta^i_{xy} \in [\pi/4 - \alpha/2, \pi/2 - \alpha]$, and $\beta \in [\beta^i_{xy}, \pi/2[$.

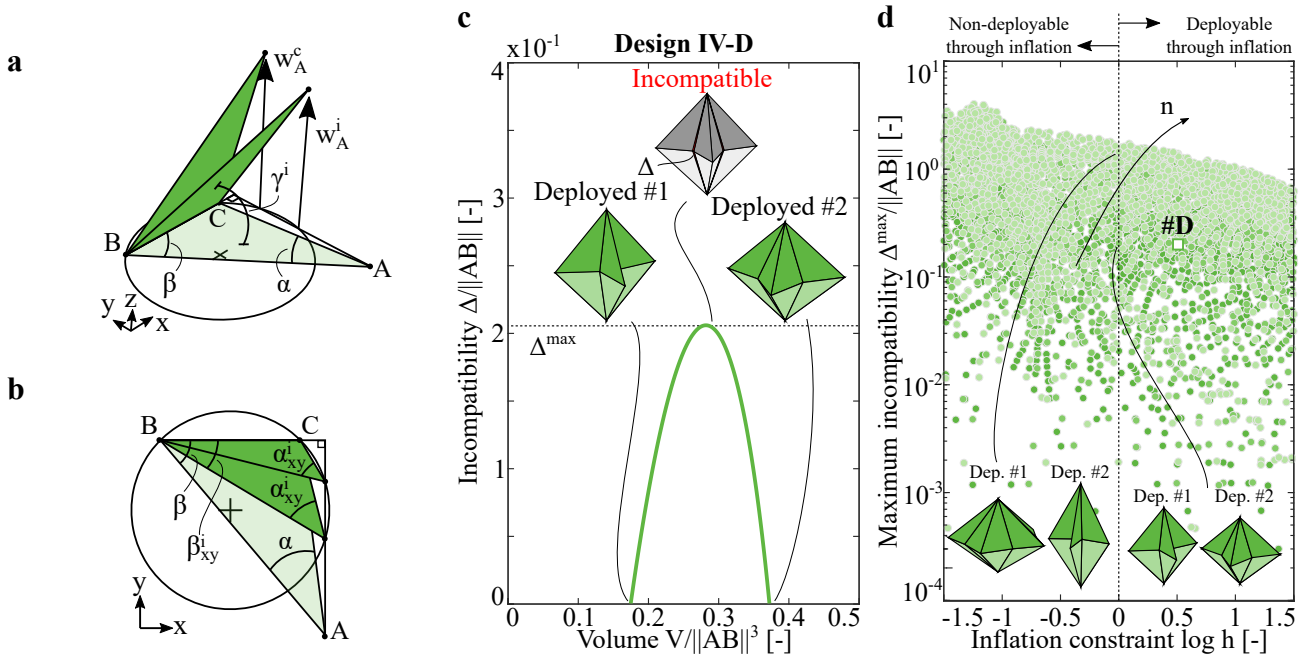

Fig. S14. Designs IV. (a-b). Isometric and projected views of the triangular building block used to create Design IV-D. **(c)**. Evolution of the incompatibility, Δ, as a function of the internal volume, V, for Design IV-D. **(d)**. Maximum incompatibility, Δ^{max} vs. inflation constraint, $\log h$ for $500,000$ different Designs IV geometries for increasing value of symmetry fold, n.

S2. Fabrication

In this study, we fabricate both centimeter-scale and meter-scale origami structures. This section gives details of the fabrication methodology used for the two considered scales.

A. Geometry and material selection. The main structures built in this study include four simple centimeter-scale origami designs, i.e. Designs I-A, II-B, III-C, and III-D, as well as two meter-scale functional designs, i.e. the archway and the shelter. Designs I-A and II-B are both chosen because they maximize the geometric incompatibility of their respective class while still being inflatable to their expanded stable state, i.e. $\log h = 0$. Design III-C is chosen with incompatibility higher than that of Design II-B—to ensure bistability—and geometry suitable for the realization of the inflatable archway (Design III-C is one of the units of our arch—see Fig.3a of the main text). Finally, we select Design IV-D to have incompatibility higher than that of Design II-B (as well as that of Design III-C) and to have two non-zero volume stable states (a property that cannot be achieved with Designs I-III).

To provide a robust and protective environment as well as to accommodate geometric frustration during deployment and minimize bending energy in the hinges, we build our origami structures out of stiff faces and compliant hinges. To realize centimeter-scale structures, inspired by recent works [24, 25], we use two different methods based on cardboard and 3D-printed faces. In the first method, we connect laser-cut cardboard faces with a double-sided adhesive sheet to form the hinges. The cardboard structures can be fabricated quickly and inexpensively to validate the compatible shapes coming from our design methodology. However, they do not provide an airtight cavity to perform experimental testing. To realize inflatable prototypes, in the second method, we assemble centimeter-scale structures by connecting faces 3D-printed out of a standard rigid material (polyactic acid) with flexible polyester laser-cut sheets to form the hinges. For the meter-scale model, we use corrugated plastic sheets for the faces as they are available in large format (8 ft $\times$ 4 ft, 4-mm thick) and have high bending stiffness to weight ratio because of the corrugation. To form the compliant hinges, we reduce the thickness of the material locally by scoring the plastic sheet (see archway pattern in Fig. S20). In the case of the shelter, we also engrave the sheets (reducing the thickness on an area rather than a single line) to further increase the compliance compliance to the hinges to allow geometric frustration during the deployment (see shelter pattern in Fig. S20). Details on each fabrication technique are provided below.

B. Centimeter-scale structures.

Structures with cardboard faces. In the first method, we assemble laser-cut cardboard facets with double-sided adhesive tape to form the hinges (see Fig. S15). Below are the eight steps needed to fabricate a cardboard sample (see Fig. S16 and Video S1):

- **Step 1:** we cut the different components of the origami structure out of 0.25-mm thick cardboard sheets (Bristol pad from Blick) with a 150 W laser-cutter (PLS6.150D from Universal Laser Systems), using both lasers at 30% power, 30% speed, and 1000 pulses per inch (**Step 1a**). **Step 1b:** we obtain a first sheet with trapezoidal shapes cut out to later accommodate for connection tabs (see **Step 3**). **Step 1c:** we obtain another sheet with trapezoidal shapes both cut out and patterned to later accommodate for connection pockets and tabs (see **Step 3**). Note that the circular holes are for alignment purposes (see **Steps 2** and **3**).
- **Step 2:** we insert the cut sheet obtained in **Step 1b** on an alignment platform and place double-sided adhesive tape (0.05-mm thick sheet from Graphix) on the origami parts.
- **Step 3:** we overlay the sheet obtained in **Step 1c** on top of the sheet with adhesive to create two layers of triangular facets connected by adhesive tape to form the hinges. Note the tabs and pockets now have exposed adhesive for connection.
- **Step 4:** we place the two assembled sheets in the laser cutter at the same location using the alignment circular holes.
- **Step 5:** we cut out the perimeter of the origami patterns on the sheets with the laser-cutter and obtain two hinged triangular facet layers with tabs and pockets for connection.
- **Step 6:** we align the two layers and fold the tabs on the corresponding pockets to create a closed origami structure.
- **Step 7:** we insert inlets (for fluidic supply) on two of the faces (designed with an additional hole to accommodate it).
- **Step 8:** we deploy the origami structure from the flat stable state to the expanded stable state.

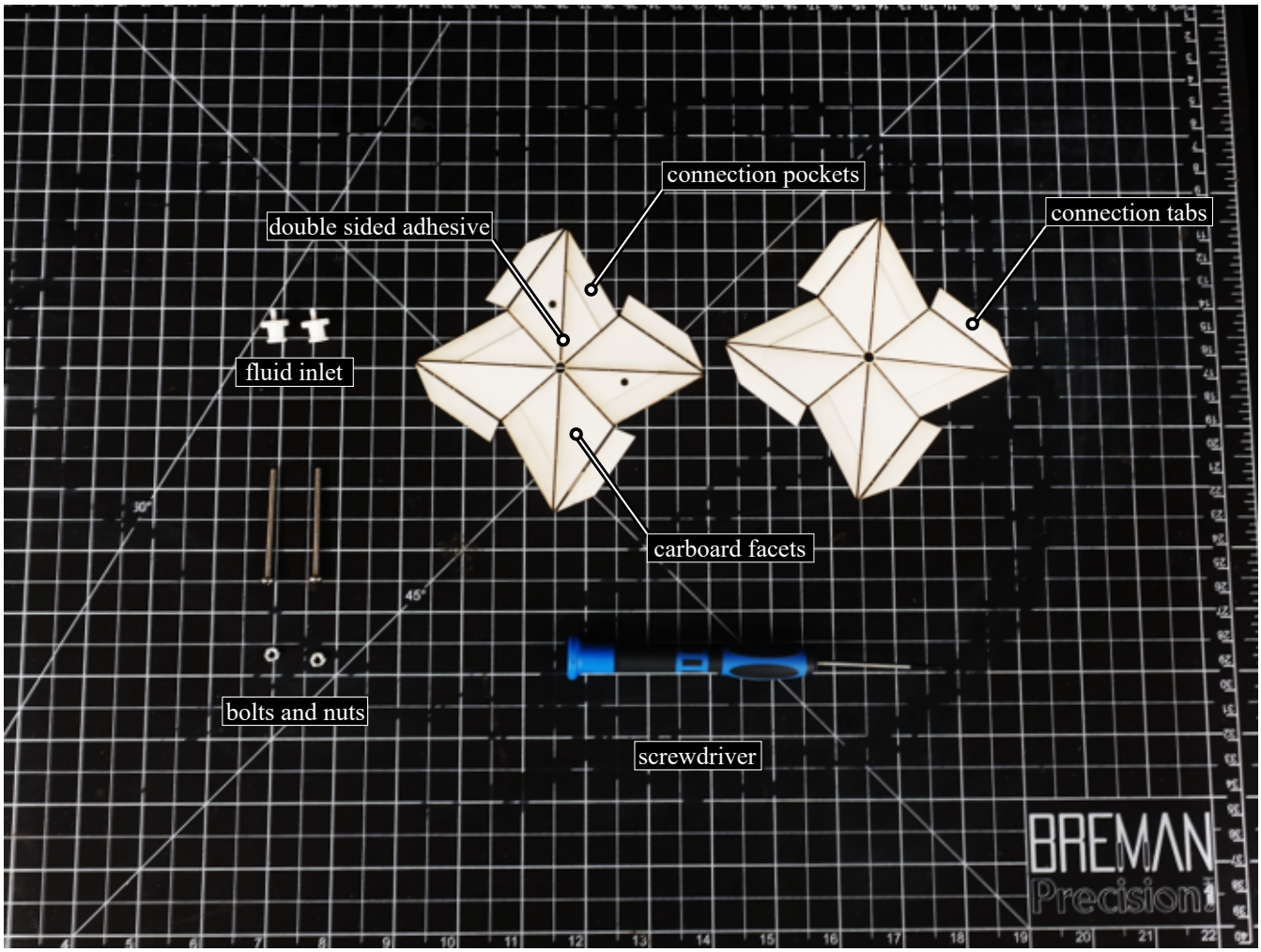

Fig. S15. Toolkit of the centimeter-scale origami structures with cardboard facets. The tools required to build the centimeter-scale origami structures out of cardboard facets and double-sided adhesive tape hinges.

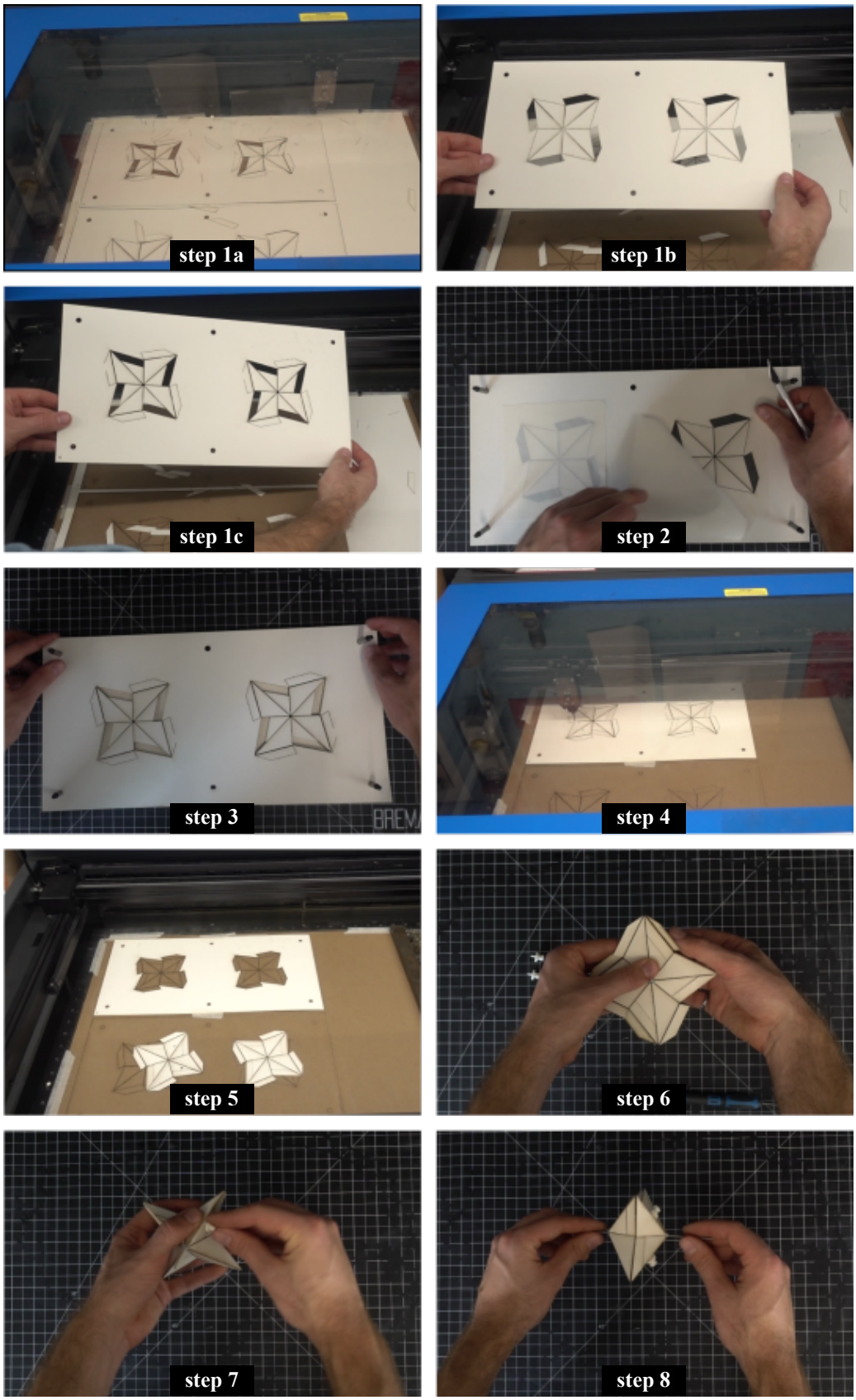

Fig. S16. Centimeter-scale fabrication with cardboard facets. Snapshots of the eight steps required to fabricate the centimeter-scale origami structures with cardboard facets.

Structures with 3D-printed faces. To realize inflatable prototypes, we assemble centimeter-scale structures by connecting 3D-printed faces with flexible laser-cut sheets to form the hinges (see Fig. S17).

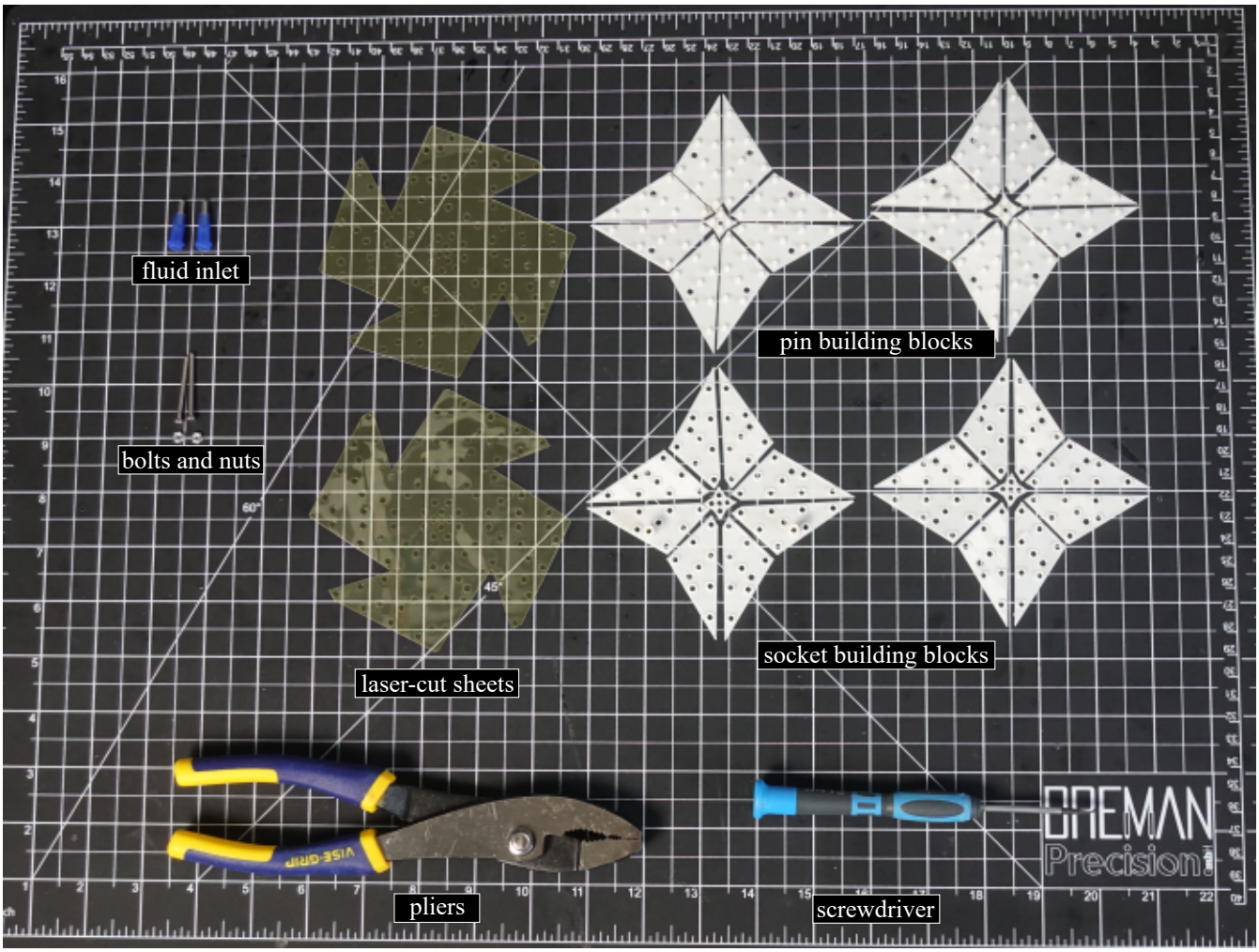

Fig. S17. Toolkit of the centimeter-scale origami structures with 3D-printed facets. The tools required to build the centimeter-scale origami structures with 3D-printed facets.

For each face of the structure, we 3D-print two 0.5-mm thick layers (3D Universe 2.85 mm white PLA filament bundle) using an Ultimaker 3 with a 0.25 mm print core with slight modifications to the *fine* default settings (travel acceleration lowered to 2000 mm/s^2). Note that to facilitate assembly one layer has a set of pins printed on one of its surfaces, whereas the other has sockets. The polyester sheets (0.002-in thick polyester film from McMaster-Carr) are cut with a 150 W laser-cutter (PLS6.150D from Universal Laser Systems), using both lasers at 8% power, 30 % speed, and 1000 pulses per inch. To connect faces together and form a complete origami structure, we snap the pin and socket connections on the 3D-printed parts together using pliers. Note that to obtain optimal bonding between the faces we use pins with height and diameter equal to 1.5 mm and 2.65 mm, respectively, and ring sockets with height, internal, and external diameters equal to 0.5 mm, 2.8 mm, 4.3 mm, respectively. Finally, to seal the origami structure, we coat it in the deployed state with a 0.5 mm-thick layer of silicone rubber (Ecoflex 00-30 from Smooth-On). Below are the eight steps needed to fabricate a sample (see Fig. S18):

- **Step 1:** we 3D-print 0.5-mm thick faces with pins and sockets out of polyactic acid (3D Universe 2.85 mm white PLA filament bundle) using a Ultimaker 3.
- **Step 2:** we laser-cut 0.002-in thick polyester sheets with a 150 W laser-cutter (PLS6.150D from Universal Laser Systems). Note that holes to allow for the pin-socket connections are embedded into the sheets.
- **Step 3:** we insert an inlet (for fluidic supply) on one of the faces (designed with an additional socket to accommodate it) and snap the corresponding face with pins, while lying the laser-cut sheet in the middle.

- **Step 4:** we arrange on the two laser-cut sheets half of the faces (all oriented in the same direction as the face with the inlet in **Step 3**) and snap them together.
- **Step 5:** we insert another inlet (for pressure measurement) on a face designed with an additional socket to accommodate it. Note that this face is symmetric to the previous ones already snapped.
- **Step 6:** we arrange on the two laser-cut sheets the remaining half of the faces (all oriented in the same direction as the face with the inlet in **Step 5**) and snap them together to form the closed origami structure in the flat stable state.
- **Step 7:** we manually deploy the origami to its expanded stable state.
- **Step 8:** we coat the origami structure with a thin layer of silicone rubber (Ecoflex 00-30 from Smooth-On), hang it, and let it cure for three hours at room temperature. Note that we repeat the coating process twice and apply two layers.

In **Section 1**, we demonstrated that we can design bistable and inflatable origami shapes with flat and expanded stable states. However, our prototypes have a non-zero rest angle in the initial stable state due to bending energy introduced in the hinges during fabrication. This rotation of the faces in the initial state is largely determined by the manufacturing technique used to realize the samples. To emphasize this point, in Fig. S19, we report the initial and expanded stable configurations for Design II-B (characterized by $(\alpha^{(1)}_{\text{II-B}}, \beta^{(1)}_{\text{II-B}}) = (43.6^\circ, 25.2^\circ)$ and $(\alpha^{(2)}_{\text{II-B}}, \beta^{(2)}_{\text{II-B}}) = (46.4^\circ, 33.5^\circ)$) with cardboard and 3D-printed faces. While both samples show identical deployed stable configurations, their initial state is quite different. The cardboard structure is initially almost flat, but is not airtight (and therefore not inflatable). Differently, the silicone rubber layer that makes the sample with 3D-printed faces airtight (and therefore inflatable) leads to a more pronounced rotation of the faces in the initial state.

C. Meter-scale structures. All meter-scale structures tested in this study are made out of corrugated plastic sheets (clear 8 ft $\times$ 4 ft, 4-mm thick corrugated plastic sheets from Corrugated Plastics). The origami patterns are formed on the sheets using a digital cutting system (G3 cutter from Zünd). Note that for the inflatable arch we use a scoring operation (cutting through 75% of the material along a single line) to create compliant hinges that allow for the geometric incompatibility during deployment. However, to account for the larger amount of incompatibility in the shelter design, in addition to scoring, we engrave the sheets (removing 75% of the material on a localized zone with an engraver) to create hinges with extra compliance. The cutting patterns for the inflatable archway and emergency shelter are shown in Fig. S20.

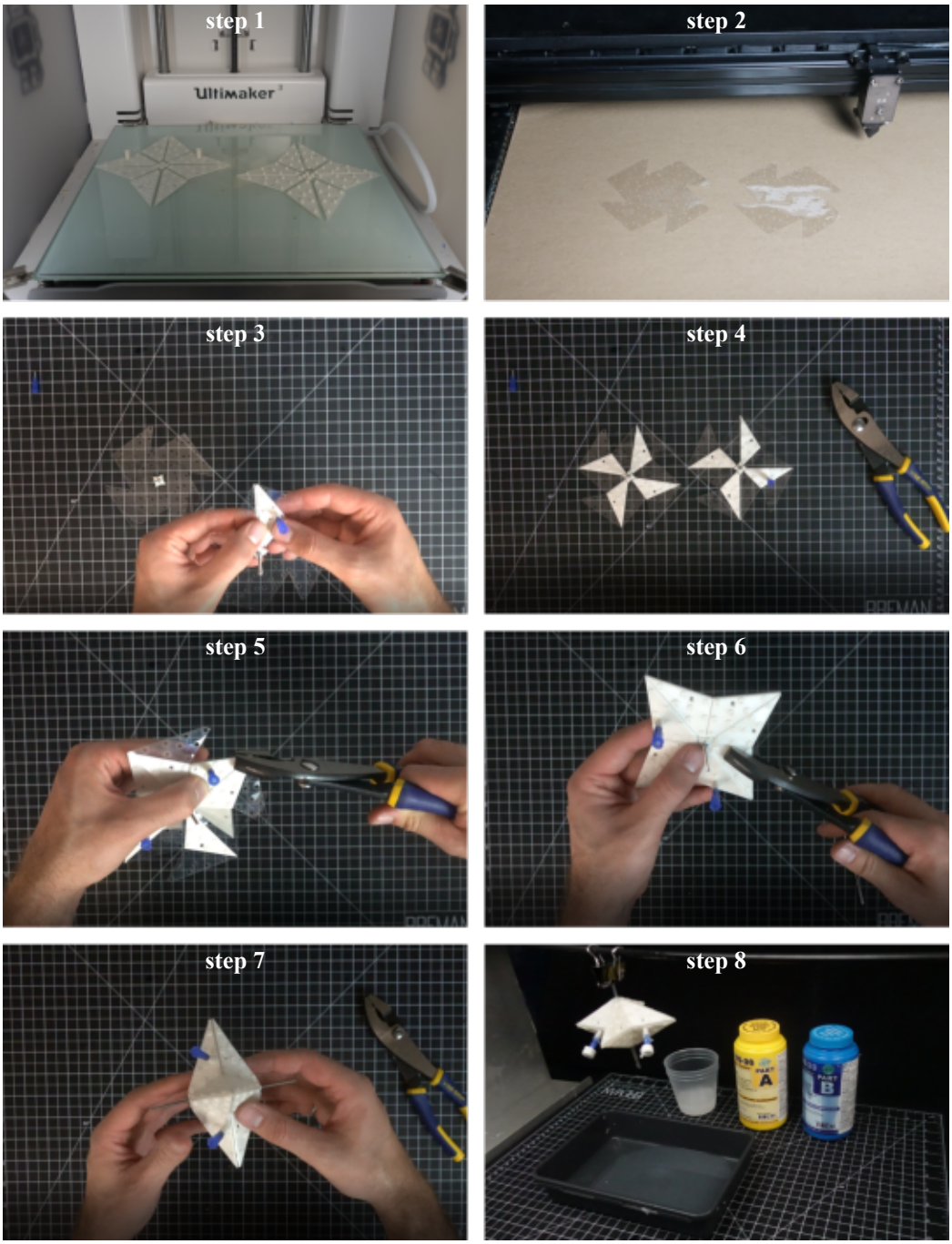

Fig. S18. Centimeter-scale fabrication with the 3D-printed facets. Snapshots of the eight steps required to fabricate the centimeter-scale origami structures with the 3D-printed facets.

Once the sheets are cut, we assemble them using adhesive tape (transparent duct tape from 3M) to form an airtight cavity. As an example, our meter-scale origami shelter is fabricated using the following 20 steps (see Fig. S21 and Video S4):

- **Step 1:** we cut and score the corrugated plastic sheet using a digital cutting system (G3 cutter from Zünd).
- **Step 2:** we lay down the eight main panels of the meter-scale shelter assembled out of the cutting patterns in Figs. S20c-g.
- **Step 3:** we apply adhesive tape to the scored hinges to seal the main panels.
- **Step 4:** we assemble the sheets together to form the eight main panels of the meter-scale shelter.
- **Step 5:** we combine two of the main panels together by applying adhesive tape in the flat position.

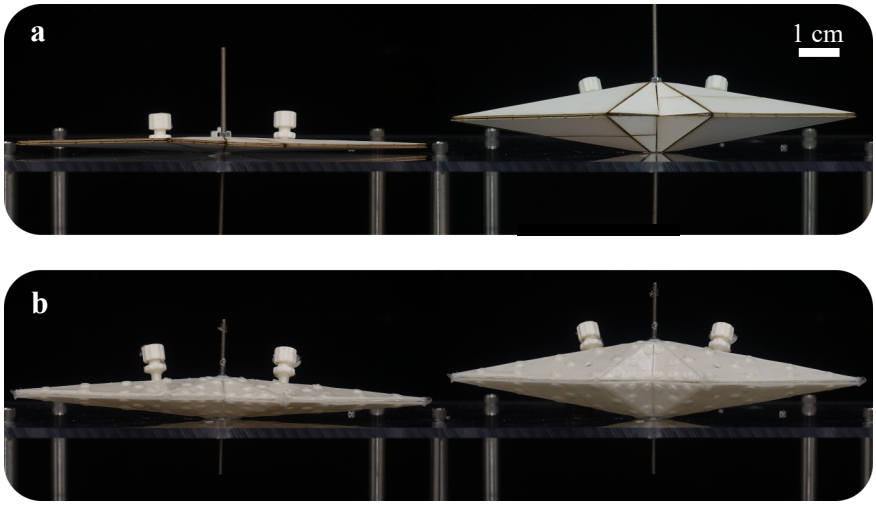

Fig. S19. Initial state for our sample. One of the stable states of our origami shapes can be designed to be geometrically flat. However, the fabricated structures exhibit a rest angle in the flat state due to the bending energy introduced in the hinges during fabrication as well as the finite thickness of the facets. Here, we show the stable flat state and deployed state of Design II-B (characterized by $(\alpha^{(1)}_{\text{II-B}}, \beta^{(1)}_{\text{II-B}}) = (43.6^\circ,\ 25.2^\circ)$ and $(\alpha^{(2)}_{\text{II-B}},\ \beta^{(2)}_{\text{II-B}}) = (46.4^\circ,\ 33.5^\circ)$) fabricated with cardboard (**a**) and 3D-printed facets (**b**). While both samples show identical deployed stable configurations, their initial state is quite different. The cardboard structure is initially almost flat, but is not airtight (and therefore not inflatable). Differently, the Ecoflex layer that makes the sample with 3D-printed faces airtight (and therefore inflatable) leads to a more pronounced rotation of the faces in the initial state.

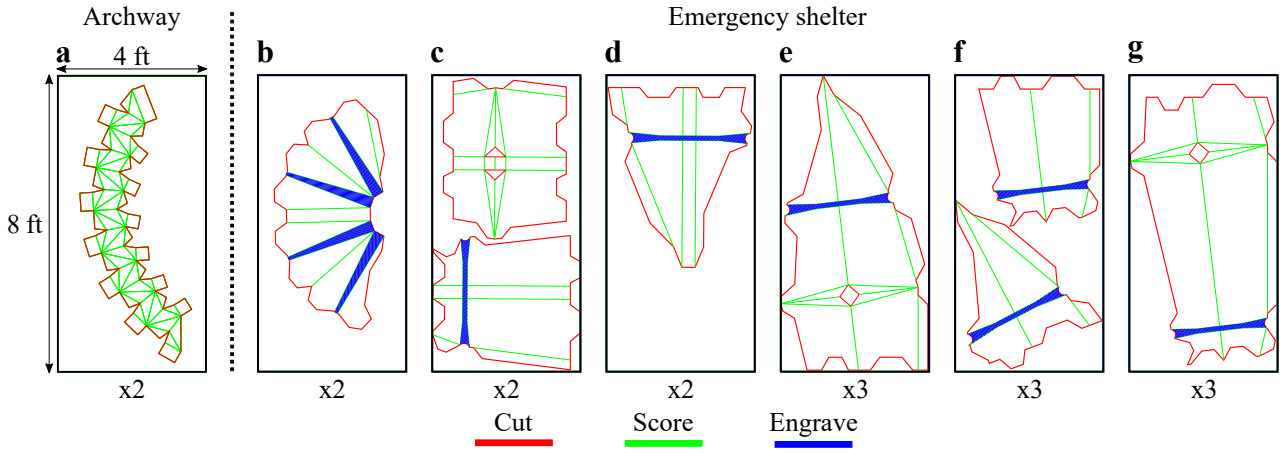

Fig. S20. Digital cutting patterns of the meter-scale archway and emergency shelter. **(a)**. The archway is fabricated out of two identical cutting patterns where the red and green lines represent through cuts to release the parts and scoring operations to make the hinges, respectively. **(b-g)**. The emergency shelter is assembled from six different cutting patterns that make the roof, walls, and floor of the structure. Here the red, green, and blue lines represent cutting, scoring, and engraving operations, respectively. Note that the latter give additional compliance to the hinges to allow geometric frustration during the deployment.

- **Step 6:** we deploy these two main panels to finish assembling them.
- **Step 7:** we repeat Steps **5** and **6** on the next two panels.
- **Step 8:** we assemble the first four panels to form half of the structure.
- **Step 9:** we repeat Steps **5-8** to form the second half of the structure
- **Step 10:** we combine the two halves.
- **Step 11:** we apply adhesive tape to the scored hinges to seal the two panels forming the roof of the structure (assembled out of the cutting pattern in Fig. S21b).
- **Step 12:** we attach the roof to the rest of the structure with adhesive tape to form the complete closed shelter.

- **Step 13:** we cut through one of the main panels using a guide to create the door of the shelter.
- **Step 14:** we cut a hole in the bottom part of the shelter and fix a plastic tube for fluid supply.
- **Step 15:** we connect the shelter to a vacuum pump.
- **Step 16:** we deflate the shelter to the flat stable state.
- **Step 17:** we fold the shelter flat.
- **Step 18:** we bring the shelter back up and connect it to a pressure pump.
- **Step 19:** we inflate the shelter to the deployed stable state.
- **Step 20:** we disconnect the pressure supply and the shelter remains deployed.

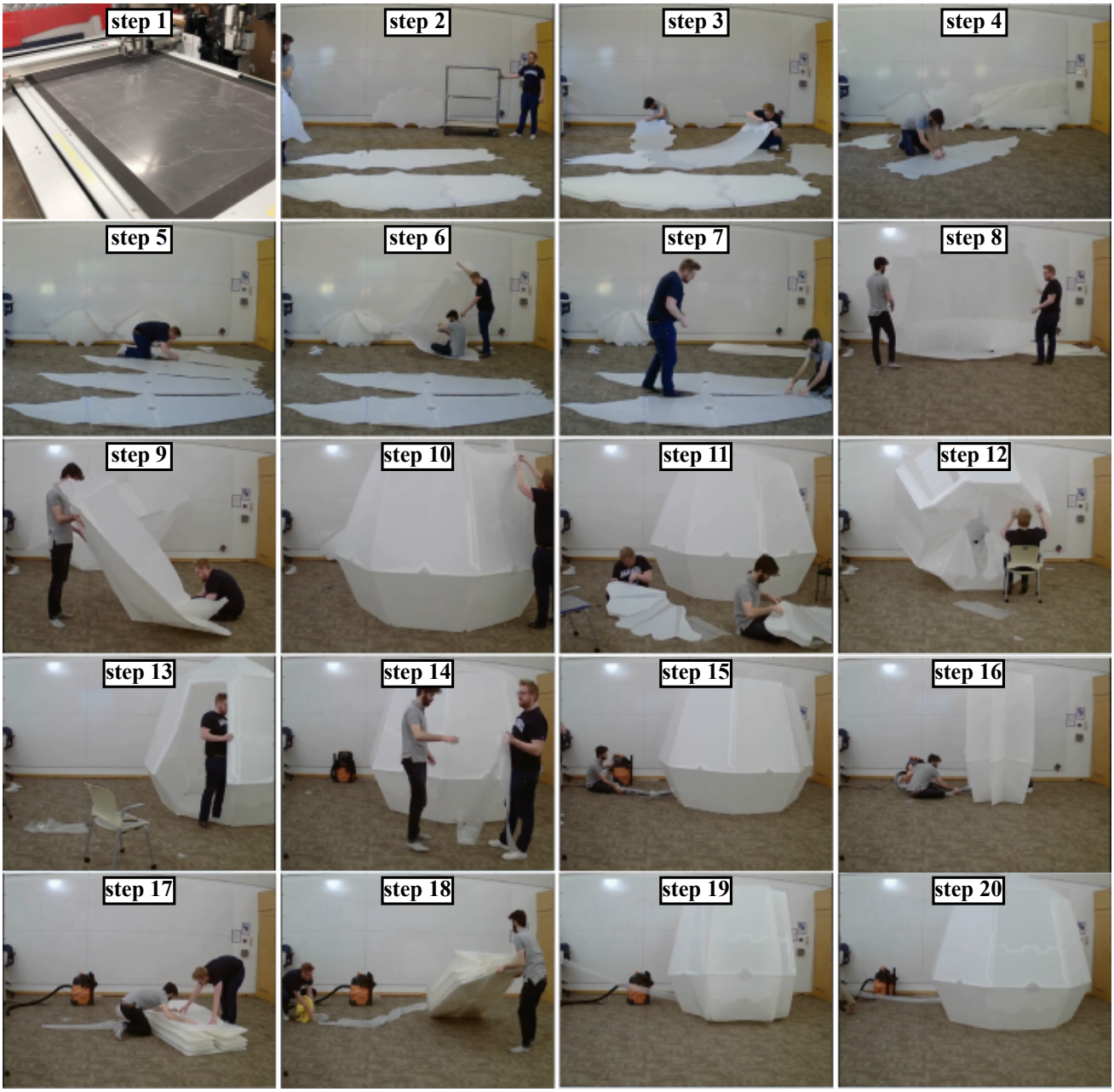

Fig. S21. Meter-scale fabrication. Snapshots of the 20 steps required to fabricate the meter-scale origami shelter.

S3. Testing

To characterize the response of the fabricated centimeter-scale origami structures, we inflate them with water— to eliminate the influence of air compressibility— and measure their pressure-volume relation. As shown in Fig. S22, we use a syringe pump (Pump 33DS, Harvard Apparatus) to displace water into the origami structure at 10 mL/min and measure the pressure using a pressure sensor (MPXV7002DP with a measurement range of ±2 kPa and MPXV7025DP with a measurement range of ±25 kPa, both by NXP USA). Note that we submerge the entire structure in a water tank to eliminate the influence of gravity while eliminating air from all supply tubes and calibrating the pressure to atmospheric pressure before each measurement cycle.

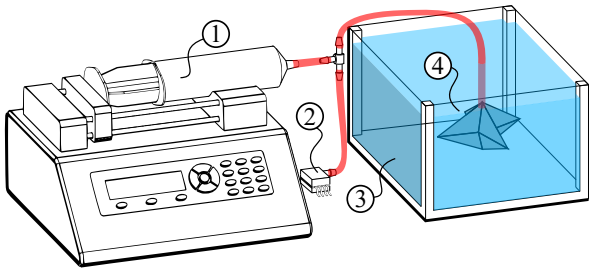

Fig. S22. Experimental setup of the inflation with water. Schematic of the test setup used to characterize the pressure-volume curve of the origami structures with (1) syringe pump, (2) pressure sensor, (3) water tank, and (4) origami structure.

In Fig. S23, we report the experimentally measured pressure-volume curves for Designs I-A, II-B, III-C, and IV-D. To validate repeatability, we test for each design three specimens and report the mean (solid lines) and standard deviation (shaded region). In addition to the pressure-volume curves, we also report the energy-landscape of each structure (dashed lines), obtained by integrating numerically the pressure-volume curves as

$$\mathcal{E} = \int \bar{p} \mathrm{d}\bar{V}, \qquad [44]$$

where $\bar{p}$ and $\bar{V}$ are the average pressure and volume measured during our tests. We find that for Design I-A (Fig. S23a), the energy landscape is convex with a single minimum at $V = 0$ (identifying a monostasble structure). All other three designs are bistable as they exhibit brief period of negative pressure and an energy landscape with two local minima. Note that the energy profile of bistable structures is characterized by two energy barriers: the first one describes the energy cost for a structure to reach the stable expanded configuration and the second one the energy cost to snap back to its initial state.

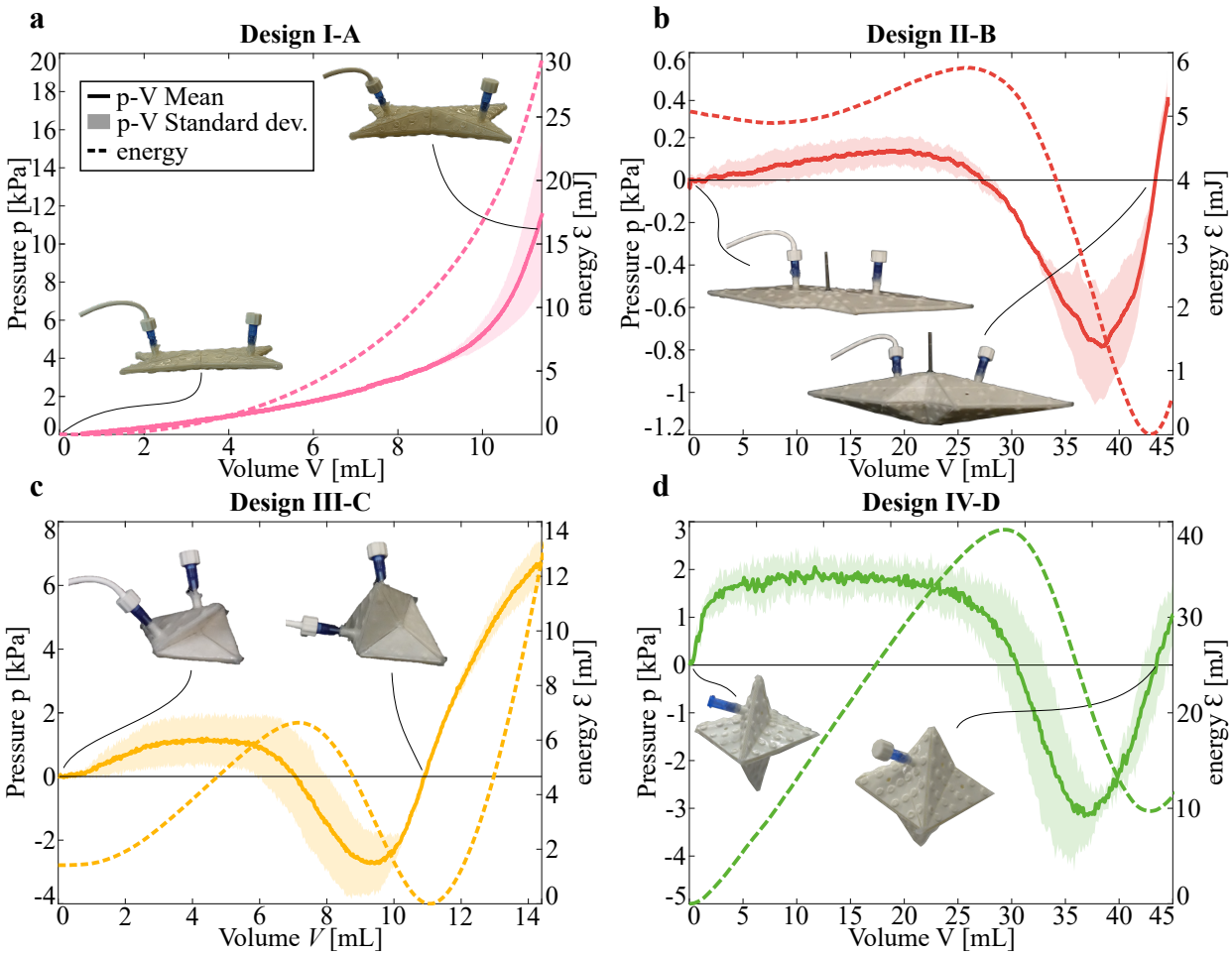

Fig. S23. Experimental pressure-volume curves of our origami structures. (a-d). Measured pressure vs. volume relationships and numerically integrated energy vs. volume curves for Designs I-A, II-B, III-C, and IV-D. We test for each design three specimens and report the mean pressure-volume curve (solid lines) with its standard deviation (shaded region) as well as the energy-volume curve (dashed lines) numerically integrated from the mean pressure-volume curve. Note that the initial non-zero pressure peak of Design II-B is coming from noise filtering of the pressure signal.

S4. Additional results

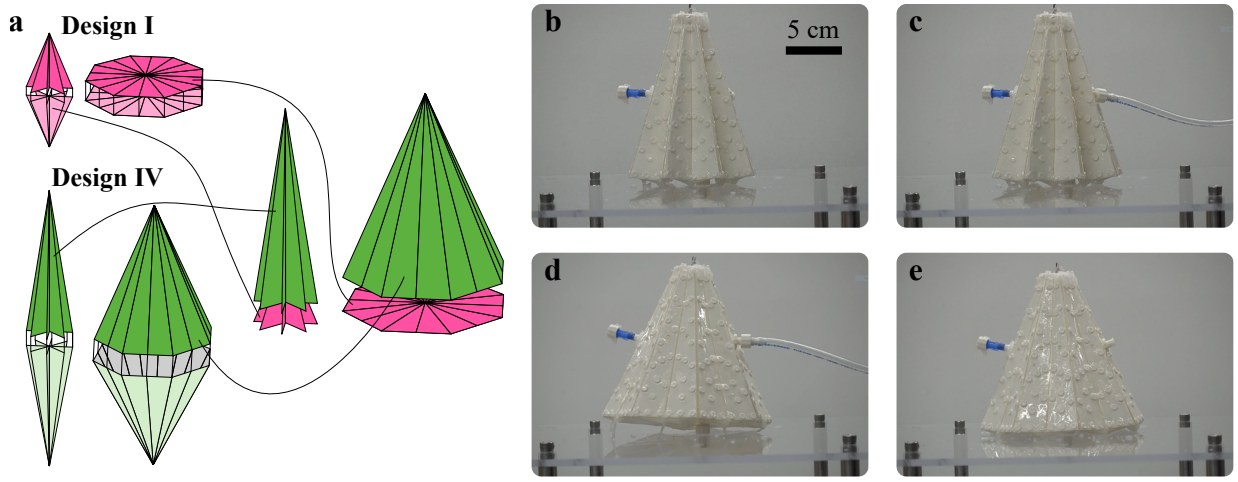

Fig. S24. Inflatable tent-like design. (a). By combining one layer of a Design I with $(\alpha_{\mathrm{I}}^{(1)}, \beta_{\mathrm{I}}^{(1)}) = (45°, 45°)$ and $(\alpha_{\mathrm{I}}^{(2)}, \beta_{\mathrm{I}}^{(2)}) = (45°, 45°)$ with another one of a Design IV with $(\alpha_{\mathrm{IV}}^{(1)}, \beta_{\mathrm{IV}}^{(1)}) = (10°, 80°)$ and $(\alpha_{xy}^{i}, \beta_{xy}^{i}) = (45°, 45°)$, we can create an inflatable tent-like cavity. **(b)**. Centimeter-scale prototype with near zero volume in the initial stable state. Note that due to the finite thickness of the material, the initial state is not completely flat foldable. **(c)**. We connect the prototype to a pressure supply. **(d)**. Upon inflation, the tent-like design snaps into the deployed position. **(e)**. Even after releasing the pressure, because of its bistability, the tent-like design remains in the deployed position.

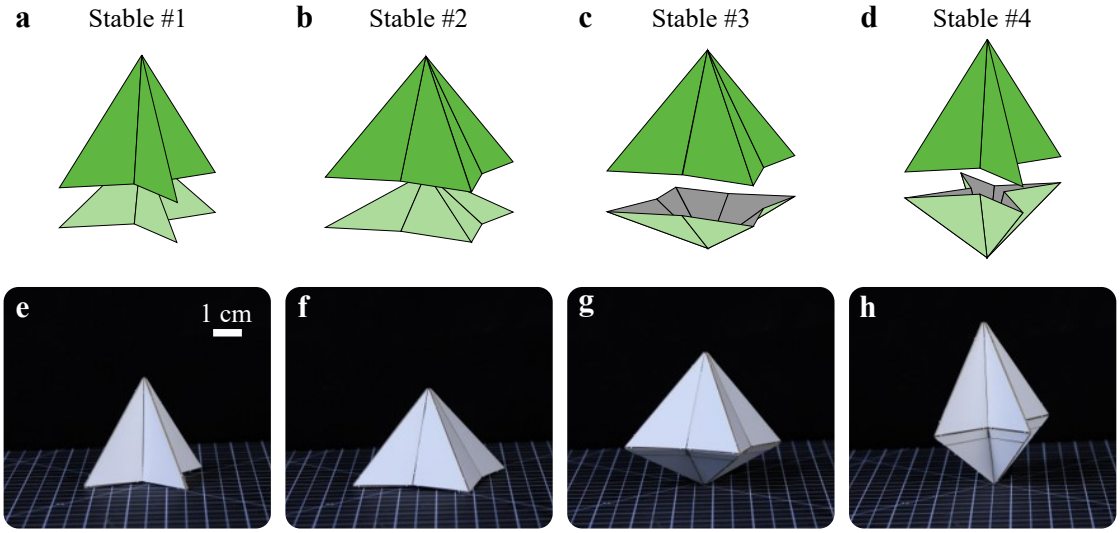

Fig. S25. Multistable origami shapes. Our design methodology can be used to realize origami shapes with more than two stable states. **(a-d)**. By merging a layer of a Design IV unit with $(\alpha_{\mathrm{IV}}^{(1)}, \beta_{\mathrm{IV}}^{(1)}) = (29°, 56°)$ and $(\alpha_{xy}^{i}, \beta_{xy}^{i}) = (45°, 35°)$ with another one of a different Design IV unit with $(\alpha_{\mathrm{IV}}^{(1)}, \beta_{\mathrm{IV}}^{(1)}) = (40°, 42°)$ and $(\alpha_{xy}^{i}, \beta_{xy}^{i}) = (45°, 35°)$, we can obtain an origami shape with four stable states. **(e-h)**. The four stable states of a fabricated centimeter-scale prototype.

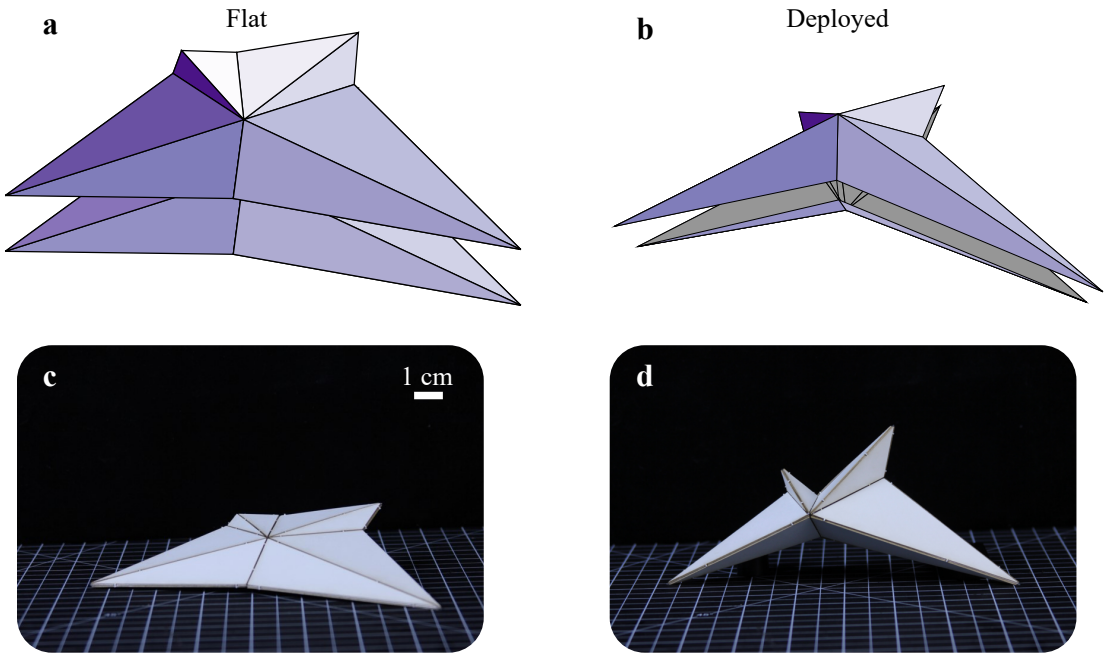

Fig. S26. Closed origami structure comprising eight different triangles. We can further increase our design space by connecting more than two different triangles. **(a-b)**. Flat and deployed compatible states of an origami design comprising eight different triangles with $(\alpha^{(k)}, \beta^{(k)}) = (55°, 30°)$, $(21°, 40°)$, $(48°, 24°)$, $(68°, 17°)$, $(64°, 21°)$, $(57°, 22°)$, $(57°, 22°)$, $(15°, 52°)$, and $(32°, 49°)$ for $k = 1, \ldots, 8$. **(c-d)**. Flat and deployed stable states of a fabricated centimeter-scale prototype.

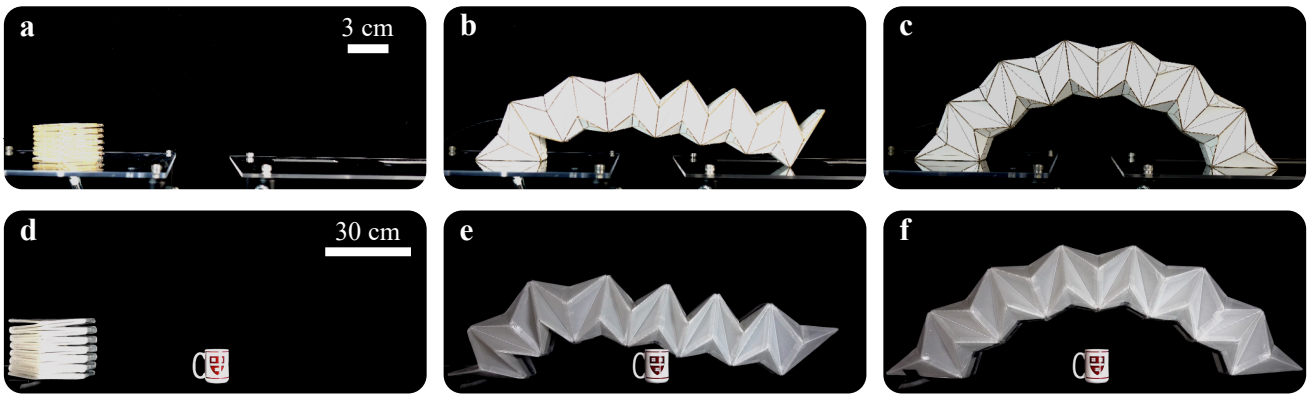

Fig. S27. Deployment of centimeter and meter-scale arches. The deployment of centimeter-scale (**a-c**) and meter-scale (**d-f**) arches is qualitatively similar.

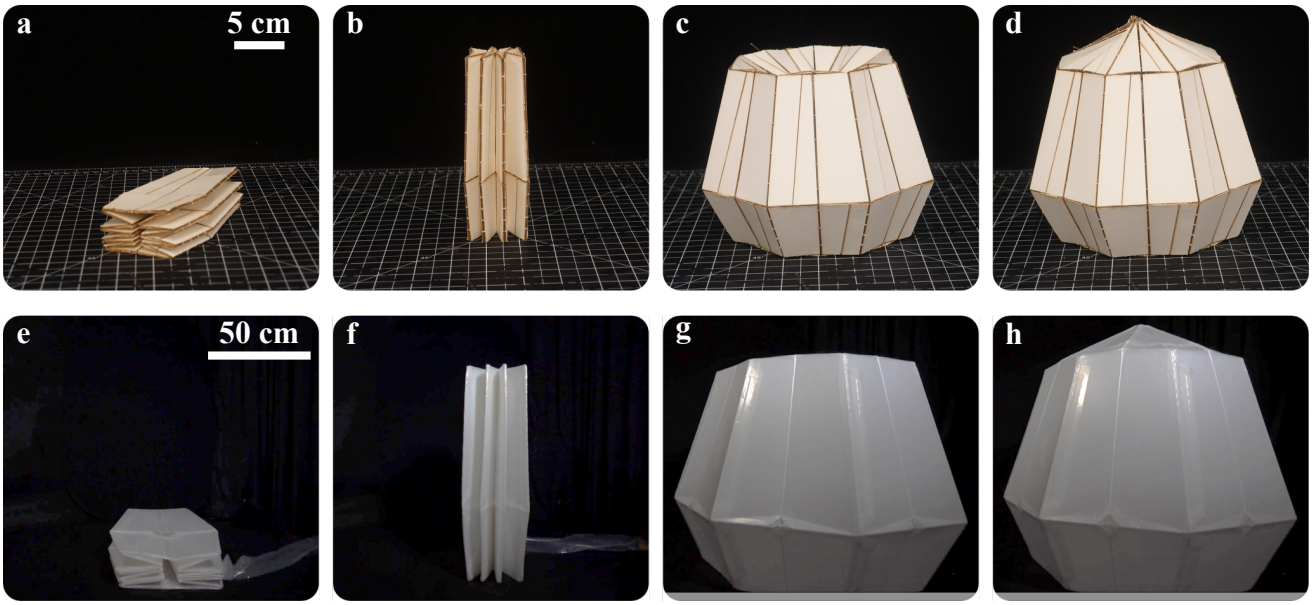

Fig. S28. Deployment of centimeter and meter-scale shelters. The deployment of centimeter-scale (**a-d**) and meter-scale (**e-h**) shelters is qualitatively similar.

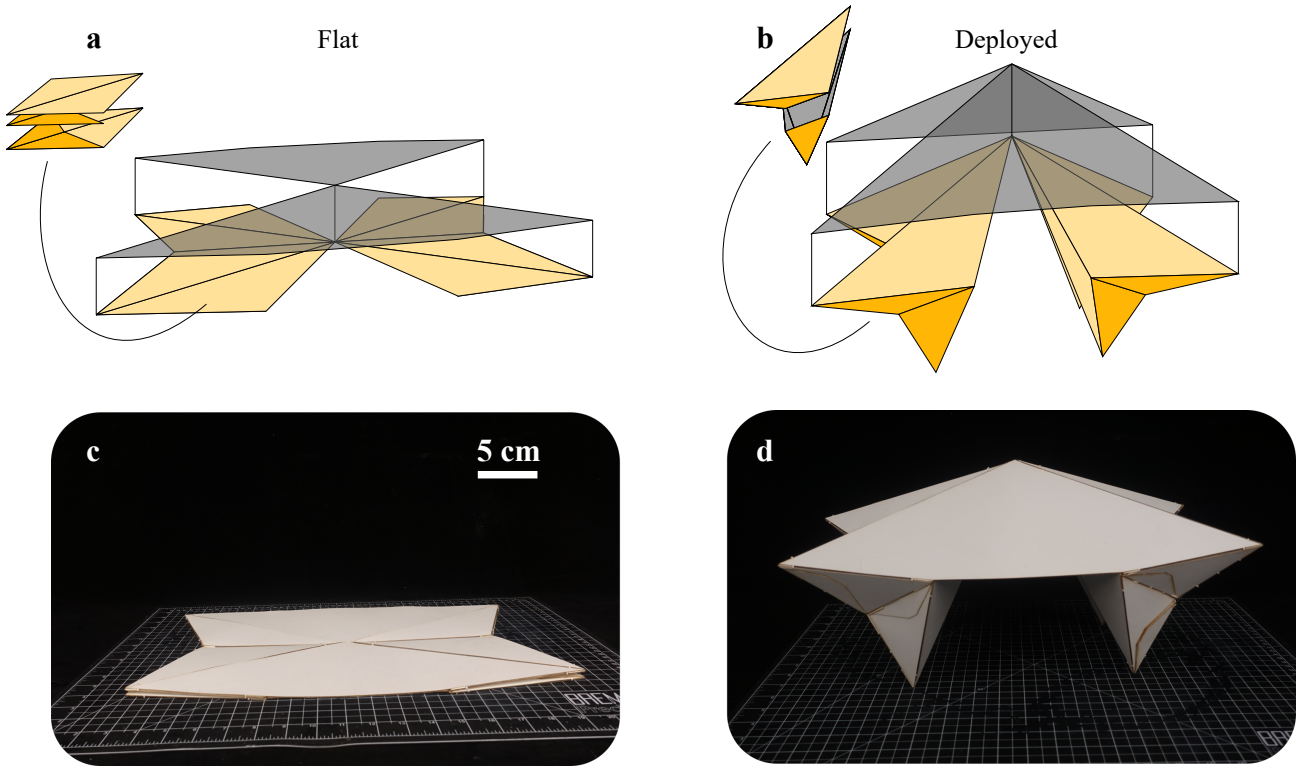

Fig. S29. A deployable pagoda-like structure. By assembling four identical Design III units, we can obtain a deployable pagoda-like structure. **(a-b)** Flat and deployed states of an origami design comprising four identical Design III units with $(\alpha_{III}^{(1)}, \beta_{III}^{(1)}) = (37^\circ, 30^\circ)$ and $(\alpha_{III}^{(2)}, \beta_{III}^{(2)}) = (37^\circ, 40^\circ)$. Note that the grey panels in **(a-b)** are added both for aesthetic reasons and to provide additional support. **(c-d)**. Flat and deployed stable states of a fabricated centimeter-scale prototype.

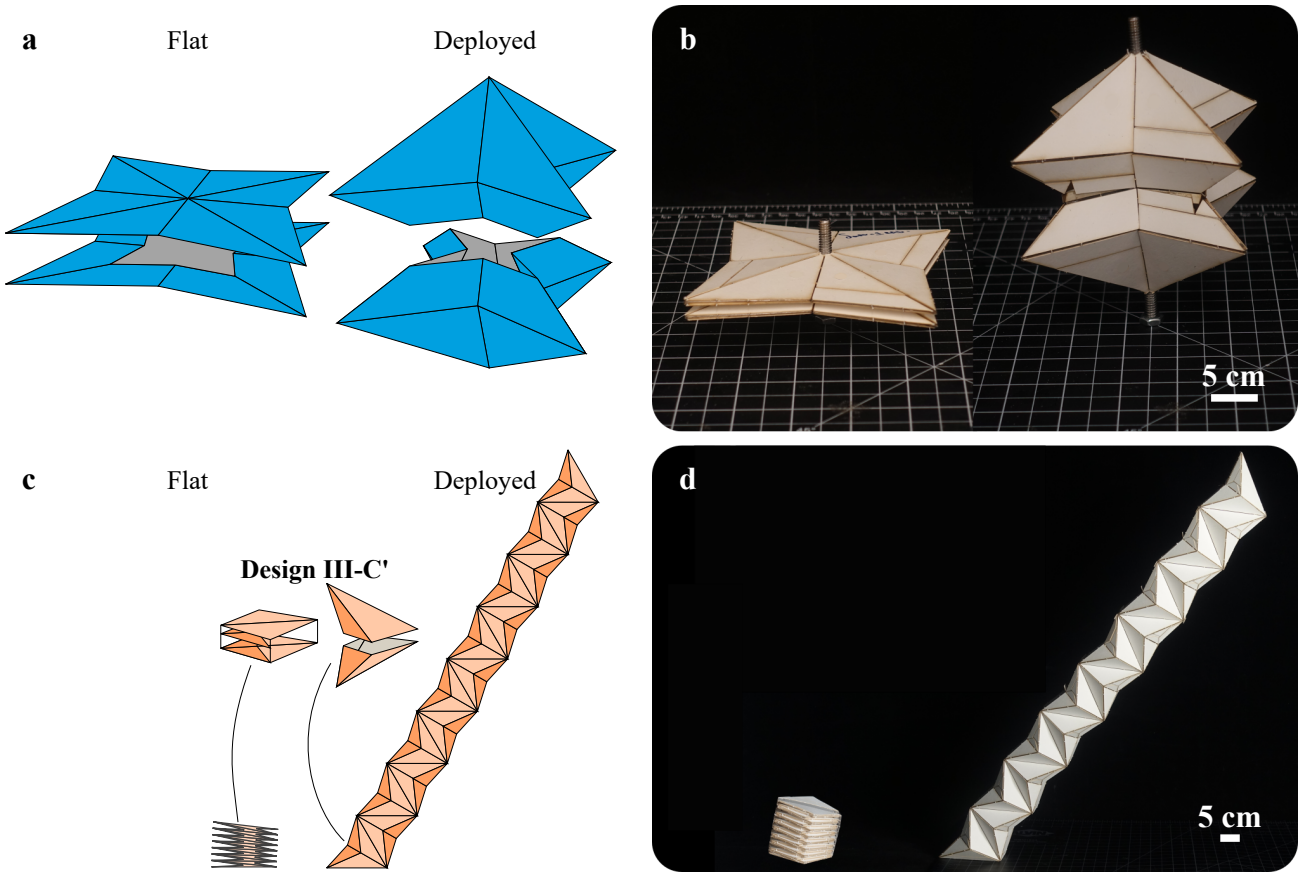

Fig. S30. Deployable booms. (a-b). By stacking Design I units, we can obtain a deployable boom. **(a)**. Flat and deployed states of an origami boom design realized by connecting two Design I units with $(\alpha_I^{(1)}, \beta_I^{(1)}) = (\alpha_I^{(2)}, \beta_I^{(2)}) = (45°, 32°)$. Note that to avoid single point contact during assembly, we cut the units at 25 % of their deployed height and connect them with the tabs and pockets system described in **Section 2A**. **(b)**. Flat and deployed stable states of a fabricated centimeter-scale prototype. **(c-d)**. By assembling Design III units, we can obtain a bistable and inflatable boom. **(c)**. Flat and deployed states of an origami boom comprising 15 identical Design III units with parameters $(\alpha_{\text{III-C}'}^{(1)}, \beta_{\text{III-C}'}^{(1)}, \alpha_{\text{III-C}'}^{(2)}, \beta_{\text{III-C}'}^{(2)})$ = $(30°, 37°, 30°$, and $51°)$. **(d)**. Flat and deployed stable states of a fabricated centimeter-scale prototype.

Video S1. Fabrication of centimeter-scale structures. To realize centimeter-scale structures, we use two different methods based on cardboard and 3D-printed faces. In the first method, we assemble laser-cut cardboard facets with double-sided adhesive tape to form the hinges. In the second approach, we connect 3D-printed faces with flexible laser-cut sheets to form the hinges and coat the structures with a thin layer of silicone rubber to create an airtight cavity.

Video S2. Inflatable and bistable origami shapes. In an attempt to design inflatable origami structures with flat and expanded stable configurations, we create a library of shapes realized by assembling two different triangles.

Video S3. Multistable inflatable origami structures at the meter-scale. By combining our library of bistable origami shapes, we build meter-scale structures that (*i*) transform from a compact shape to an expanded one; (*ii*) deploy and retract through a single pressure input; (*iii*) harness multistability to lock in place after deployment; and (*iv*) provide a robust enclosure through their stiff faces.

Video S4. Fabrication of the meter-scale shelter. The meter-scale shelter is fabricated out of 8 ft X 4 ft, 4-mm thick, corrugated plastic sheets. We use a digital cutting system to cut the different parts of the shelter and pattern the hinges by scoring the sheets to reduce the thickness locally. To create an inflatable cavity, we connect the cut parts with adhesive tape.